ESI for

Homochiral Hierarchical Molecular Assemblies through Dynamic Combination of Conformational States of a Single Chiral Building Block at the Liquid/Solid Interface

Matsuhiro Maeda, Kazuya Sato, Steven De Feyter, Kazukuni Tahara

This file includes:

1. Syntheses of cDBA-OC14(*S*)-OH and cDBA-OC14(*R*)-OH

1.1 General Methods

Commercially available *N*,*N*-dimethylformamide (DMF) and ^{i}PrOH were distilled and stored with molecular sieves 3 Å and 4 Å, respectively, priori to use. THF and CH_2Cl_2 were passed through activated alumina and copper catalysts in a Glass Contour solvent purification system before use. Other commercially available chemical reagents were used as received. Tris(*tert*-butyldimethylsilyloxy)tris(methoxymethoxy)dehydrobenzo[12]annulene **DBA-OTBS-OMOM** was prepared following the reported procedure.[1]

A JEOL ECA-500 spectrometer was used for the ^{1}H (500 MHz) and ^{13}C (125 MHz) NMR measurements. The ^{1}H and ^{13}C NMR spectra were referenced to tetramethylsilane signals (0.00 ppm) in $CDCl_3$. Recycling HPLC separation was undertaken with a JAI LC-5060 recycling chromatograph using 600 mm × 20 mm JAIGEL-1HR and 2HR GPC columns with $CHCl_3$ as the eluent. HPLC analysis with an Cholester column (Nacalai tesque, COSMOSIL Cholester, 4.6 mm × 150 mm) was performed using a SHIMADZU LC-20AD system with a SPD-M20A photodiode array detector. A SHIMADZU LC-20AR system with a SPD-20A detector was used for the preparative scale HPLC separation with a Cholester column (Nacalai tesque, COSMOSIL Cholester, 20 mm × 250 mm). Other spectra were recorded using the following instruments: IR spectra, JACSCO FT/IR-410; mass spectra, JMS-T100GCV (TOF). As the heat sources for the reactions, oil baths were used.

Synthesis of **cDBA-OC14(*S*)-OH** and **cDBA-OC14(*R*)-OH** from **DBA-OTBS-OMOM** is summarized in Scheme S1.[2]

Scheme S1. Syntheses of **cDBA-OC14(*S*)-OH** and **cDBA-OC14(*R*)-OH**.

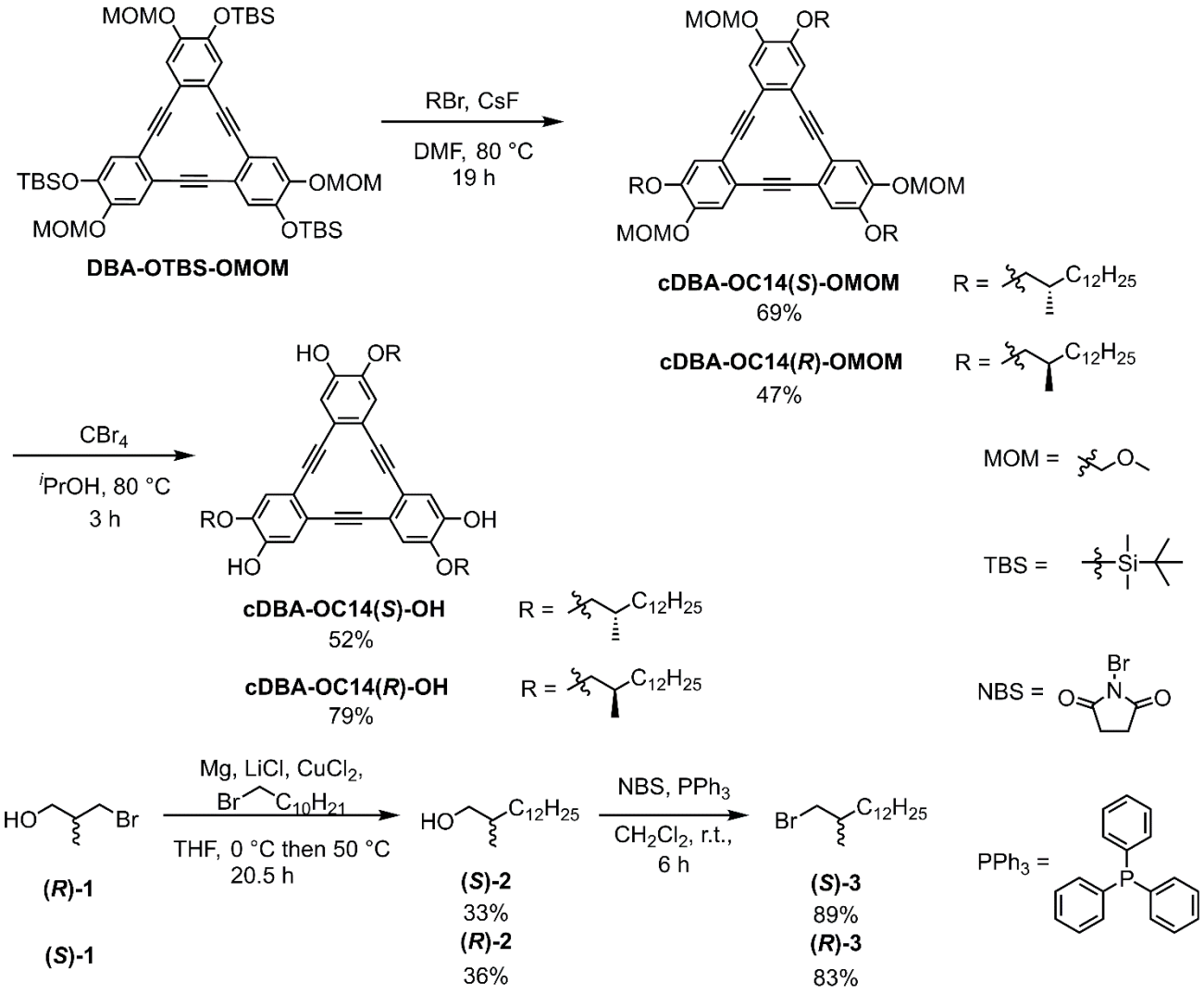

1.2 Synthesis of (*S*)-2-Methyltetradecan-1-ol (*S*)-2

Under argon atmosphere, to a suspension of magnesium (1.41 g, 58.1 mmol) in THF (30.0 mL) in a reaction vessel, 1-bromoundecane (6.50 mL, 28.7 mmol) was added. The mixture was stirred at room temperature for 40 min. This mixture was used as a Grignard reagent. In parallel to the preparation of the Grignard reagent, $CuCl_2$ (532 mg, 3.95 mmol), LiCl (308 mg, 7.26 mmol), and THF (6.45 mL) were added to another reaction vessel under argon atmosphere in an ice bath. To this reaction vessel in an ice bath, the Grignard reagent was added. Then, (*R*)-3-bromo-2-methyl-1-propanol (480 μL, 4.58 mmol) was added to the mixture, and the mixture was stirred at 50 °C for 19.5 h. The reaction was quenched by the addition of sat. NH_4Cl aq. The reaction mixture was diluted with water. Reaction

products were extracted with ether, and the organic phase was washed with brine and dried over $MgSO_4$. After evaporation of the solvents under vacuum, the crude mixture was subjected to a silica gel column chromatography (hexane/AcOEt = 5/1) to afford compound **(*S*)-2** (371 mg, 36% yield) as a colorless oil. NMR spectra of compound **(*S*)-2** agreed with those in a previous report.[3] ^{1}H NMR (500 MHz, $CDCl_3$, 25 °C) δ 3.54–3.48 (m, 1H), 3.46–3.39 (m, 1H), 1.65–1.56 (m, 1H), 1.43–1.18 (m, 22H), 1.15–1.05 (m, 1H), 0.92 (d, *J* = 6.5 Hz, 3H), 0.89 (t, *J* = 7.0 Hz, 3H); ^{13}C NMR (125 MHz, $CDCl_3$, 25.0 °C) δ 68.5, 35.8, 33.2, 31.9, 30.0, 29.68, 29.66, 29.4, 27.0, 22.7, 16.6, 14.1.

1.3 Synthesis of (*R*)-2-Methyltetradecan-1-ol (*R*)-2

Except for the reaction time for the preparation of a Grignard reagent (60 min) in the synthesis of **(*S*)-2**, the same procedure was used for the synthesis of compound **(*R*)-2**. From (*S*)-3-bromo-2-methyl-1-propanol (310 μL, 2.96 mmol), compound **(*R*)-2** (222 mg, 33% yield) was obtained as a colorless oil. NMR spectra of compound **(*R*)-2** agreed with those in a previous report.[3] ^{1}H NMR (500 MHz, $CDCl_3$, 25 °C) δ 3.51 (dd, *J* = 10.5, 6.0 Hz, 1H), 3.42 (dd, *J* = 11.0, 7.0 Hz, 1H), 1.64–1.56 (m, 1H), 1.44–1.04 (m, 23H), 0.92 (d, *J* = 7.0 Hz, 3H), 0.88 (t, *J* = 7.0 Hz, 3H); ^{13}C NMR (125 MHz, $CDCl_3$, 25.0 °C) δ 68.5, 35.8, 33.2, 31.9, 30.0, 29.68, 29.66, 29.4, 27.0, 22.7, 16.6, 14.1.

1.4 Synthesis of (*S*)-1-Bromo-2-methyltetradecane (*S*)-3

Under argon atmosphere, compound **(*S*)-2** (330 mg, 1.44 mmol), PPh_3 (1.05 g, 4.01 mmol), and CH_2Cl_2 (5.00 mL) were added to a reaction vessel in an ice bath. *N*-Bromosuccinimide (NBS, 701 mg, 3.94 mmol) was added to the mixture which was continuously stirred. After stirring for 6 h at room temperature, the solvents were removed under reduced pressure. The crude mixture was purified with a silica gel column chromatography (hexane) to give compound **(*S*)-3** (348 mg, 83% yield) as a colorless oil. NMR spectra of compound **(*S*)-3** agreed with those in a previous report.[3] ^{1}H NMR (500 MHz, $CDCl_3$, 25 °C) δ 3.42–3.37 (m, 1H), 3.35–3.29 (m, 1H), 1.83–1.74 (m, 1H), 1.48–1.39 (m, 1H), 1.35–1.18 (m, 22H), 1.01 (d, *J* = 7.0 Hz, 3H), 0.88 (t, *J* = 7.0 Hz, 3H); ^{13}C NMR (125 MHz, $CDCl_3$, 25.0 °C) δ 41.7, 35.2, 34.9, 31.9, 29.71, 29.66, 29.6, 29.4, 26.9, 22.7, 18.8, 14.1.

1.5 Synthesis of (*R*)-1-Bromo-2-methyltetradecane (*R*)-3

Using the procedure used for the synthesis of **(*S*)-3**, compound **(*R*)-3** (253 mg, 89% yield) was obtained as a colorless oil from compound **(*R*)-2** (223 mg, 0.977 mmol). The ^{13}C NMR spectrum of compound **(*R*)-3** agreed with that in a previous report. ^{1}H NMR (500 MHz, $CDCl_3$, 25 °C) δ 3.40 (dd, *J* = 10.0, 5.0 Hz, 1H), 3.32 (dd, *J* = 9.5, 6.5

Hz, 1H), 1.83–1.74 (m, 1H), 1.48–1.37 (m, 1H), 1.36–1.11 (m, 22H), 1.01 (d, J = 7.0 Hz, 3H), 0.88 (t, J = 7.5 Hz, 3H); ^{13}C NMR (125 MHz, $CDCl_3$, 25.0 °C) δ 41.6, 35.2, 34.9, 31.9, 29.71, 29.68, 29.66, 29.64, 29.59, 29.4, 26.9, 22.7, 18.8, 14.1.

1.6 Synthesis of cDBA-OC14(*S*)-OMOM

Under argon atmosphere, **DBA-OTBS-OMOM** (63.6 mg, 73.0 μmol), compound **(*S*)-3** (182 mg, 625 μmol), and DMF (2.50 mL) were added to a reaction vessel. CsF (81.4 mg, 536 μmol) was added to the mixture at room temperature. After stirring at room temperature for 10 min, the mixture was stirred at 80 °C for 19 h. The reaction mixture was diluted with water. Reaction products were extracted with $CHCl_3$. The organic phase was washed with water and brine and dried over $MgSO_4$. After removal of the solvents by evaporation, the purification of the product was performed by a silica gel column chromatography (hexane/chloroform = 1/1) and recycling HPLC separations ($CHCl_3$) to furnish **cDBA-OC14(*S*)-OMOM** (58.2 mg, 69% yield) as a yellow oil. ^{1}H NMR (500 MHz, $CDCl_3$, 25.0 °C) δ 7.01 (s, 3H), 6.76 (s, 3H), 5.18 (s, 6H), 3.87–3.83 (m, 3H), 3.76–3.71 (m, 3H), 3.52 (s, 9H), 2.02–1.94 (m, 3H), 1.52–1.17 (m, 66H), 1.03 (d, J = 7.0 Hz, 9H), 0.88 (t, J = 7.0 Hz, 9H); ^{13}C NMR (125 MHz, $CDCl_3$, 25.0 °C) δ 149.9, 146.7, 121.7, 119.6, 119.3, 115.8, 95.4, 92.0, 91.6, 74.2, 56.3, 33.5, 33.0, 31.9, 29.2, 29.70, 29.66, 29.4, 26.9, 22.7, 17.1, 14.1; IR (KBr) 2920, 2850, 2210, 1591, 1510, 1473, 1343, 1227,1072, 969, 860, 723 cm^{-1}; HRMS (FD): m/z calcd. for $C_{75}H_{114}O_9$ (M^+) 1158.8463, Found: 1158.8445.

1.7 Synthesis of cDBA-OC14(*R*)-OMOM

cDBA-OC14(*R*)-OMOM (38.1 mg, 47% yield) was obtained as a yellow oil from **DBA-OTBS-OMOM** (61.2 mg, 70.2 μmol) and compound **(*R*)-3** (174 mg, 597 μmol) according to the procedure used for the synthesis of **cDBA-OC14(*S*)-OMOM**. In this case, additional purification was performed using HPLC (Cholester column, CH_3CN/CH_2Cl_2 = 55/45). ^{1}H NMR (500 MHz, $CDCl_3$, 25.0 °C) δ 7.00 (s, 3H), 6.76 (s, 3H), 5.18 (s, 6H), 3.88–3.81 (m, 3H), 3.77–3.69 (m, 3H), 3.52 (s, 9H), 2.03–1.94 (m, 3H), 1.52–1.17 (m, 66H), 1.02 (d, J = 7.0 Hz, 9H), 0.88 (t, J = 7.0 Hz, 9H); ^{13}C NMR (125 MHz, $CDCl_3$, 25.0 °C) δ 149.9, 146.7, 121.7, 119.6, 119.3, 115.8, 95.4, 92.0, 91.6, 74.2, 56.3, 33.5, 33.0, 31.9, 29.9, 29.70, 29.66, 29.4, 26.9, 22.7, 17.1, 14.1; IR (KBr) 2921, 2852, 2214, 1594, 1509, 1469, 1346, 1227, 1151, 1053, 980, 873, 721 cm^{-1}; HRMS (FD): m/z calcd. for $C_{75}H_{114}O_9$ (M^+) 1158.8463, Found: 1158.8475.

1.8 Synthesis of cDBA-OC14(*S*)-OH

Under argon atmosphere, **cDBA-OC14(*S*)-OMOM** (18.4 mg, 15.9 μmol) was added to a Schlenk tube. CBr_4 (9.0 mg, 29 μmol) and ^{i}PrOH (2.00 mL) were added to this reaction vessel. The mixture was stirred at 80 °C for 4.0 h. The solvent was removed under vacuum. Purification by a silica gel column chromatography ($CHCl_3$ and hexane/AcOEt = 1/1), recycling HPLC separations ($CHCl_3$), and HPLC (Cholester column, CH_3CN/CH_2Cl_2 = 55/45) gave **cDBA-OC14(*S*)-OH** (8.6 mg, 52% yield) as a brown sticky solid. ^{1}H NMR (500 MHz, $CDCl_3$, 25.0 °C) δ 6.80 (s, 3H), 6.73 (s, 3H), 5.61 (s, 3H), 3.92–3.86 (m, 3H), 3.83–3.78 (m, 3H), 2.01–1.92 (m, 3H), 1.53–1.19 (m, 69H), 1.03 (d, J = 6.5 Hz, 9H), 0.88 (t, J = 7.0 Hz, 9H); ^{13}C NMR (125 MHz, $CDCl_3$, 25.0 °C) δ 146.2, 146.0, 120.3, 119.3, 117.2, 114.5, 91.8, 91.3, 74.2, 33.5, 33.1, 32.0, 29.9, 29.7, 29.4, 26.9, 22.7, 17.1, 14.2; IR (KBr) 3544, 2914, 2855, 2206, 1607,1564, 1559, 1506, 1469, 1364, 1290, 1256, 1234, 1060, 1003, 875, 761, 741 cm^{-1}; HRMS (FD): *m*/*z* calcd. for $C_{69}H_{102}O_6$ (M^+) 1026.7676, Found: 1026.7692.

1.9 Synthesis of cDBA-OC14(*R*)-OH

Using the same procedure, **cDBA-OC14(*R*)-OH** (21.1 mg, 79% yield) was obtained as a brown sticky solid from **cDBA-OC14(*R*)-OMOM** (30.2 mg, 26.0 μmol). The reaction time was changed to 2 h. ^{1}H NMR (500 MHz, $CDCl_3$, 25.0 °C) δ 6.80 (s, 3H), 6.73 (s, 3H), 5.61 (s, 3H), 3.89 (dd, J = 9.3 Hz, 3H), 3.80 (dd, J = 8.8 Hz, 3H), 2.01–1.91 (m, 3H), 1.53–1.20 (m, 66H), 1.03 (d, J = 6.0 Hz, 9H), 0.88 (t, J = 7.0 Hz, 9H); ^{13}C NMR (125 MHz, $CDCl_3$, 25.0 °C) δ 146.1, 145.9, 120.3, 119.2, 117.2, 114.4, 91.8, 91.2, 74.2, 33.5, 33.0, 31.9, 29.9, 29.7, 29.4, 26.9, 22.7, 17.1, 14.1; IR (KBr) 3545, 2921, 2851, 2208, 1607,1563, 1510, 1471, 1367, 1294, 1257, 1234, 1063, 1003, 874, 761, 737 cm^{-1}; HRMS (FD): *m*/*z* calcd. for $C_{69}H_{102}O_6$ (M^+) 1026.7676, Found: 1026.7672.

2. Details of STM Observation

STM observation was performed at 20–26 °C using a Nanoscope IIID or V (Bruker AXS) with an external pulse/function generator (Agilent 33220A or TEXIO FGX-295) with negative sample bias. All STM images were recorded in a quasi-constant current mode. STM tips were prepared from mechanically cut Pt/Ir wire (80%/20%, diameter 0.25 mm).

For the SAMN preparation, **cDBA-OC14(*S*)-OH** or **cDBA-OC14(*R*)-OH** was dissolved in 1,2,4-

trichlorobenzene (TCB, purchased from Nacalai Tesque or TCI), 1-hexanoic acid (HA, purchased from Wako), or their mixture at various solute concentrations. These solvents were distilled before use. One of the solutions (15 or 40 μL) was poured into a homemade liquid cell attached to a freshly cleaved basal plane of a 1 cm^2 piece of highly oriented pyrolytic graphite (HOPG, grade ZYB, Momentive Performance Material Quartz Inc., Strongsville, OH). In most cases, to promote self-assembled molecular networks (SAMNs), annealing treatment at 80 °C for 3 h was applied using a sealed sample drying oven. To minimize the effect of solvent evaporation, a large amount of the sample solution (40 μL) was used. Moreover, during the annealing treatment, the liquid cell was covered with a stainless-steel lid. The total solvent loss during annealing treatment at 80 °C for 3 h was less than 5%. After the annealing treatment, the substrate was cooled down to room temperature. STM observation was completed within 3 hours after dropping the solution.

By changing the tunneling parameters during STM observations, the SAMN of the cDBAs and underneath graphite surface could be observed by changing bias voltage, respectively. The distortion of the image owing to thermal drift effects was corrected with respect to the surface lattice of the underneath graphite using the SPIP software (Scanning Probe Image Processor, SPIP, version 4.0.6 or 6.0.13, ImageMetrogy A/S, Hørsholm, Denmark). In STM images, white arrows and lines indicate the directions of the main symmetry axes of graphite and the scale bar, respectively. For each condition, more than 10 large area STM images (image sizes: 80 nm × 80 nm) were acquired per independent experimental session (within 3 h). Three independent sessions were performed at each condition to confirm reproducibility. The unit cell parameters were determined using more than 40 experimental data points from at least four calibrated STM images (image sizes: 30 × 30 nm^2 or smaller). The surface area of SAMNs which are weighted average values with the standard deviations was determined from more than 10 images in three independent experimental sessions.

The distribution of the triangular cluster size was statistically analyzed using more than 19 large-area STM images (80 × 80 nm^2 or larger). The size of the triangular cluster is classified by the number of the cDBA molecules (n) at each triangular side. Some imperfect triangular clusters in which the number of missing cDBA molecules at one of the triangular sides or corners is less than 10% are also included in the statistics. When the number of the cDBA molecules is different for three triangular sides, the larger number is used as the n value. Moreover, the triangular

clusters in which some of the interior cDBA molecules (m = 0) are missing were also counted for the statistical analysis. cDBA forms extended domains (larger than the image size of 80 × 80 nm^2) of the triangular cluster (n = 2 and 4) structures. The surface coverages of these SAMNs in the weighted average values with the standard deviations were determined.

3. Details of Molecular Mechanics (MM) and Molecular Dynamics (MD) Simulations

The geometries of **cDBA-OC14(*S*)-OH**, **cDBA-OC14(*R*)-OH**, and HA optimized by the semiempirical PM3 method using the Gaussian 16W ver 1.1 (Gaussian, Inc.) software were used for the construction of the network models. Based on the STM image, the orientation of the alkyl chains relative to the DBA π-core changed using the GaussView 6.0.16 (Gaussian, Inc.) and ViewerLite (Accelrys, Inc.) software. All MM/MD simulations were performed by the Materials Studio 2017 R2 software using the Forcite module with the COMPASS force field. These molecules were placed 0.350 nm above the first layer of a bilayer graphene sheet (interlayer distance is 0.355 nm). This two-layer graphene sheet was frozen during the simulations. A cutoff value of 2.0 nm was applied for the van der Waals interactions (Lennard-Jones type). We used the periodic boundary conditions (PBCs) which are experimentally derived unit cell parameters.

When the adsorption configurations of **cDBA-OC14(*S*)-OH** are optimized on finite bilayer graphene sheets at the single molecular level (Fig. 1c), PBCs are not applied. The edges of the finite bilayer graphene sheets are terminated by hydrogens. Its chemical formula and the lateral dimensions are $C_{19596}H_{1387}$ and 16.68 nm × 16.68 nm, respectively. The edges of the graphene sheets will not affect the optimization of the DBA molecule placed at the sheet center where it is over twice the cutoff distance from the edges.

4. **Hexagonal Structure of Achiral DBA-OC14-OH**

In our previous work, a hexagonal structure of achiral **DBA-OC14-OH** was observed at the TCB/graphite interface (Fig. S1).[4] In the hexagonal structure, chiral tetramers consist of molecules having two different conformational states (m = 2 and 3).

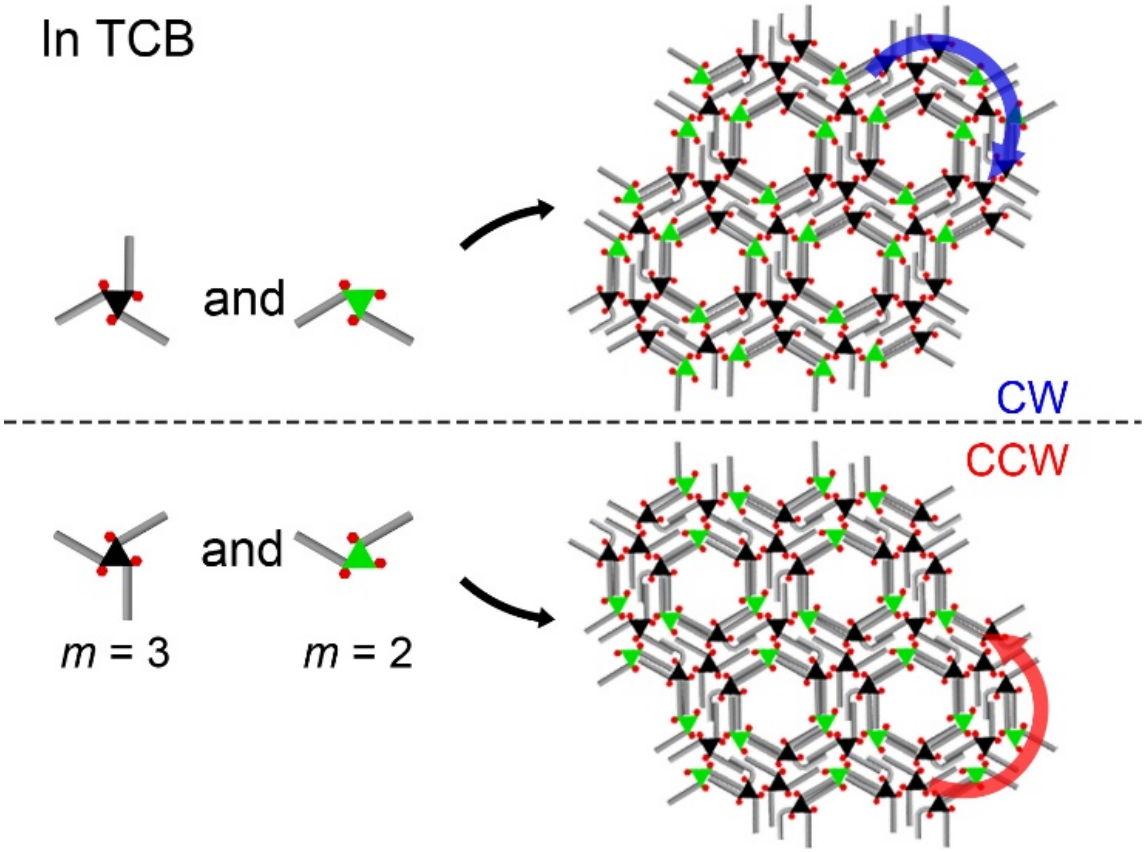

Figure S1. Schematic illustration of hexagonal structures with CW and CCW orientations formed by achiral **DBA-OC14-OH**.

5. **Supramolecular Chirality Assignment of Hierarchical Triangular Cluster Structures based on the SAMN Orientation with Respect to the Graphite Lattice**

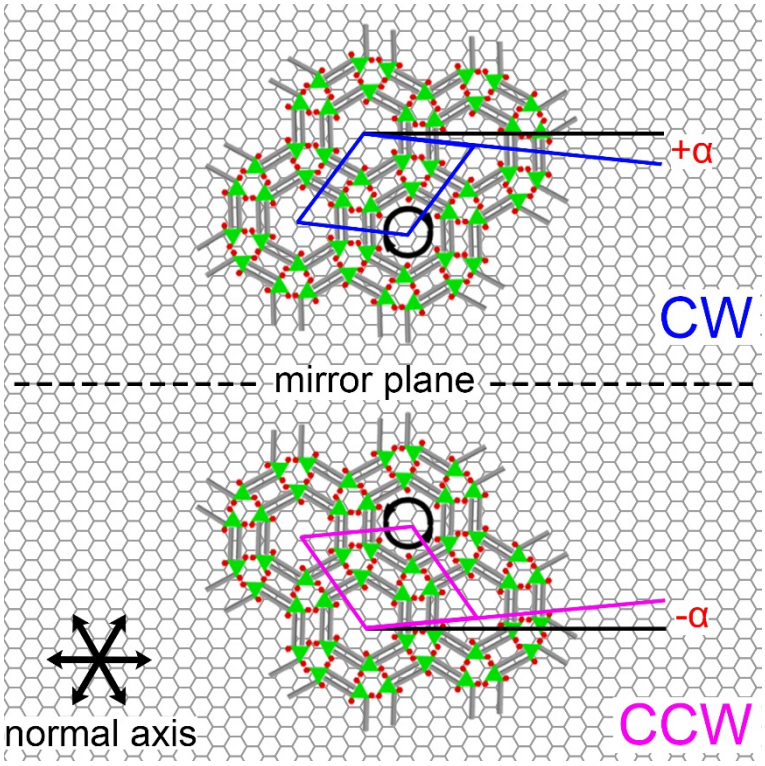

Figure S2. Schematic illustration representing the definition of angle α between the unit cell vector a and one of the normals of the main symmetry axes of graphite using triangular cluster structure $n = 2$ as a model system. The plus or minus sign of angle α determines the supramolecular chirality of SAMNs.

6. **Self-Assembly of cDBA-OC14(*S*)-OH at the TCB/Graphite Interface**

6-1. Additional STM Images

At the TCB/HOPG interface, a homochiral honeycomb structure (CCW orientation) of **cDBA-OC14(*S*)-OH** is solely observed at all solute concentrations (Fig. S3). The domain size is typically larger than the STM image dimensions (80 × 80 nm^2).

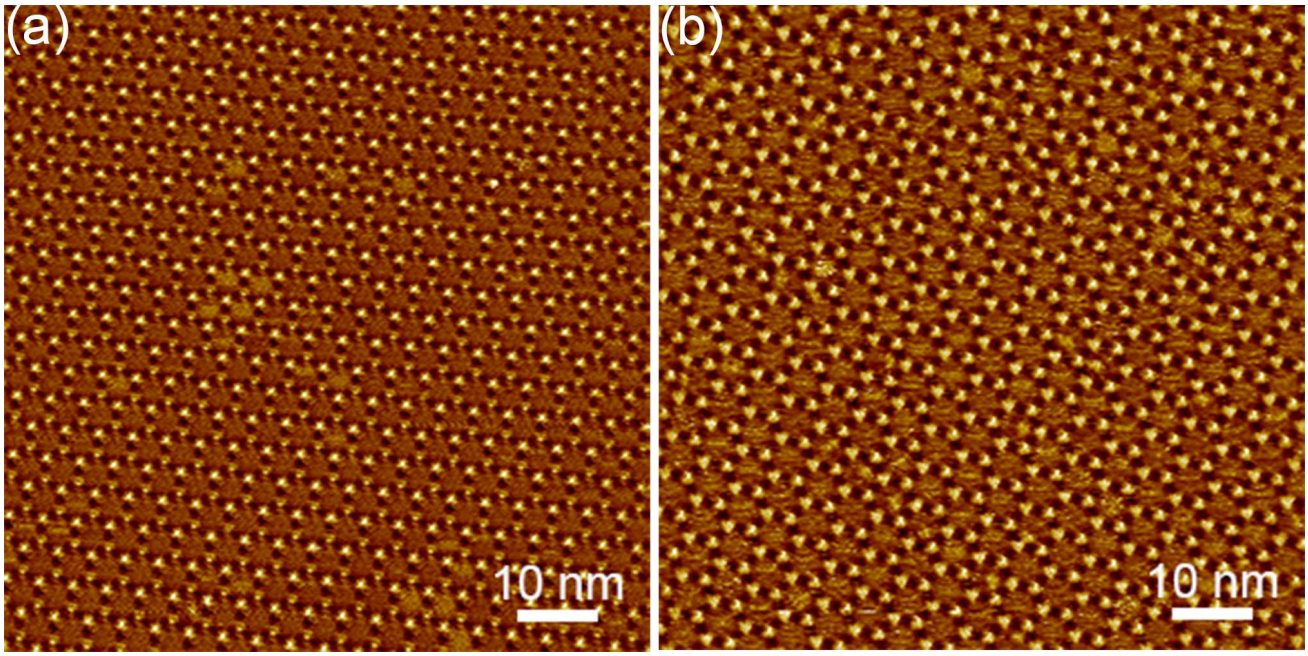

Figure S3. STM images of a homochiral honeycomb structure (a) at 3.0×10^{-6} M after annealing treatment (I_{set} = 200 pA, V_{bias} = –0.45 V) and (b) at 1.0×10^{-4} M after annealing treatment (I_{set} = 200 pA, V_{bias} = –0.66 V).

6-2. Chirality of the Honeycomb Structure of cDBA-OC14(*S*)-OH at the TCB/Graphite Interface

The unit cell parameters and angle α value of the honeycomb structure of **cDBA-OC14(*S*)-OH** at different solute concentrations were summarized in Table S1. To analyze the chirality of the honeycomb structure, more than 26 STM images (image size: 80 × 80 nm^2) were used at each condition. The supramolecular chirality of the honeycomb structure was determined by the alkyl chain orientation (CW or CCW orientation) at the rim of the hexagonal pore. The angle α value was determined using more than 30 points from more than four STM images per condition. The mean angle α values are all negative.

Table S1. Summary of Observed SAMNs at the TCB/Graphite Interfaces.

concentration (M)	annealing	observed structure	unit cell parameters and angle α value			
			a (nm)	b (nm)	γ (°)	α (°)
3.0×10^{-6} (30 images)[a]	80 °C for 3 h	honeycomb	4.99 ± 0.06	5.01 ± 0.06	60.0 ± 0.7	–10.0 ± 0.3
1.0×10^{-5} (26 images)[a]	80 °C for 3 h	honeycomb	5.00 ± 0.05	4.99 ± 0.06	60.2 ± 0.5	–10.0 ± 0.3
1.0×10^{-4} (26 images)[a]	80 °C for 3 h	honeycomb	5.01 ± 0.09	5.00 ± 0.08	50.9 ± 0.5	–9.9 ± 0.4

[a] Number of STM images used for the chirality analysis.

6-3. Energy Difference Between CW and CCW Honeycomb Structures Estimated by MM Simulations

The chirality of the honeycomb structure of **cDBA-OC14(*S*)-OH** was expressed at both the single molecular and supramolecular levels. At the single molecular level, the chirality of **cDBA-OC14(*S*)-OH** can be confirmed by the orientation of the methyl group bonded to the stereogenic centers (*up* or *down*) with respect to a surface. **cDBA-OC14(*S*)-OH**, with an *up*-methyl configuration is favored over that with a *down*-methyl configuration because of steric repulsion. By assembling the **cDBA-OC14(*S*)-OH** molecules with the *up*-methyl configuration forms a CCW honeycomb structure. Note that the supramolecular chirality, clockwise CW or CCW rotation can be differentiated by the orientations of the alkoxy chains at the rims of the pore (Fig. S4). To investigate the energy difference in the CW and CCW honeycomb structures, both structures were optimized by MM calculations with the COMPASS force field using the experimentally derived unit cell parameters as PBC conditions (Fig. S4). The total potential (E_{total}) values per DBA molecule reveal that the CCW structure is stable over the CW structure by 9.5 kcal·mol^{-1} (Figs. S4a,b).

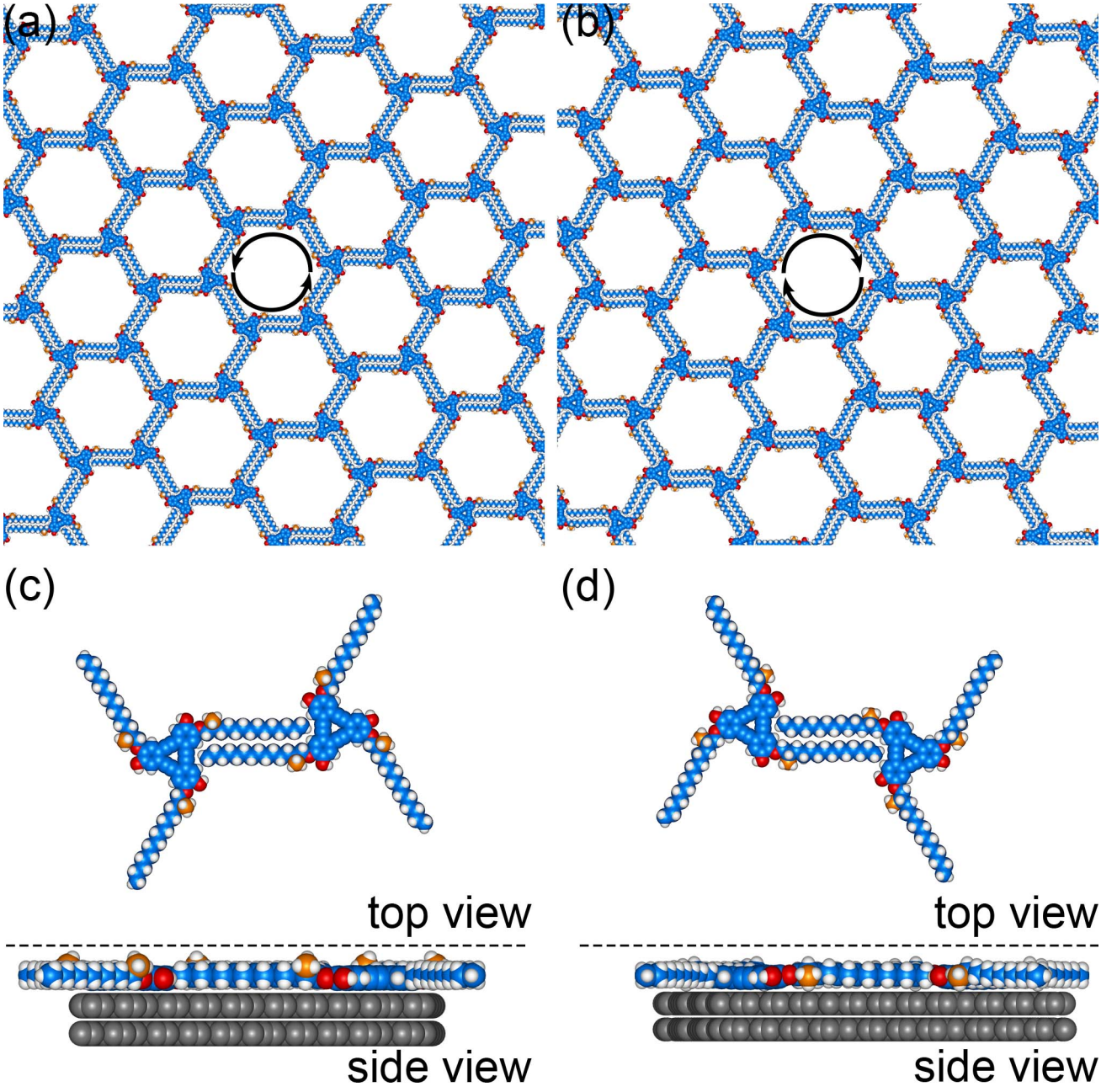

Figure S4. (a, b) MM optimized CCW and CW honeycomb structures of **cDBA-OC14(*S*)-OH** on a bilayered graphene sheet. The bilayer graphene sheets are omitted for clarity. (c, d) Chiral DBA dimers (top and side view). In the top views, the bilayer graphene sheets are omitted for clarity.

6-4. Hypothetical Models of the Tetramer of cDBA-OC14(*S*)-OH

In our previous work, a hexagonal structure of achiral **DBA-OC14-OH** was observed at the TCB/graphite interface.[4] The hexagonal structure consists of four chiral tetramers, which are composed of both chiral configurations of **DBA-OC14-OH** (one *up* and surrounding three *down* configurations and its verse versa). The tetrameric cluster consists of a C_3-symmetric DBA molecule at the center which is surrounded by three DBA molecules in a C_1-symmetric form (Fig. S5). If the central DBA adopts a favorable geometry (Fig. 1c, left), two of the alkyl chains of the other three DBA molecules would suffer from steric hindrance for their stereogenic methyl groups with the graphite surface. Hence, due to the conflicting orientations of the four cDBA molecules, the tetrameric cluster is not favored.

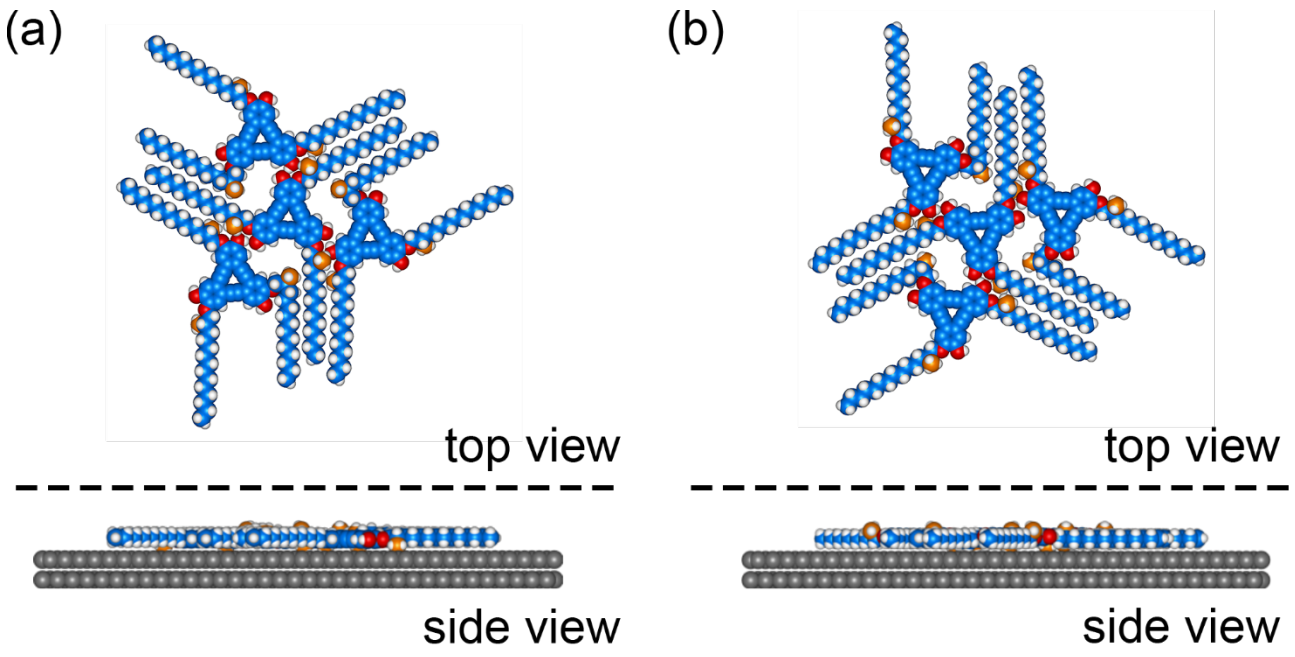

Figure S5. Top and side views of the MM (COMPASS force field) optimized hypothetical tetramers of **cDBA-OC14(*S*)-OH** on a bilayered graphene sheet. (a) The 1*up*-3*down*-tetramer and (b) 1*down*-3*up*-tetramer. In the top view, the bilayered graphene sheet was omitted for clarity.

7. Details on Self-Assembly of cDBA-OC14(*S*)-OH at the HA/Graphite Interface

7-1. An Additional STM Image of Triangular Cluster (*n* = 2) at the HA/Graphite Interface

From STM image shown in Fig. S6, the four long alkoxy chains of **cDBA-OC14(*S*)-OH** and two short alkyl fragments (red ovals) are observed between two adjacent triangular clusters (*n* = 2). We attribute these short alkyl fragments to co-adsorbed solvent HA molecules, which are hydrogen bonded to the hydroxy group(s) of the cDBA molecule.

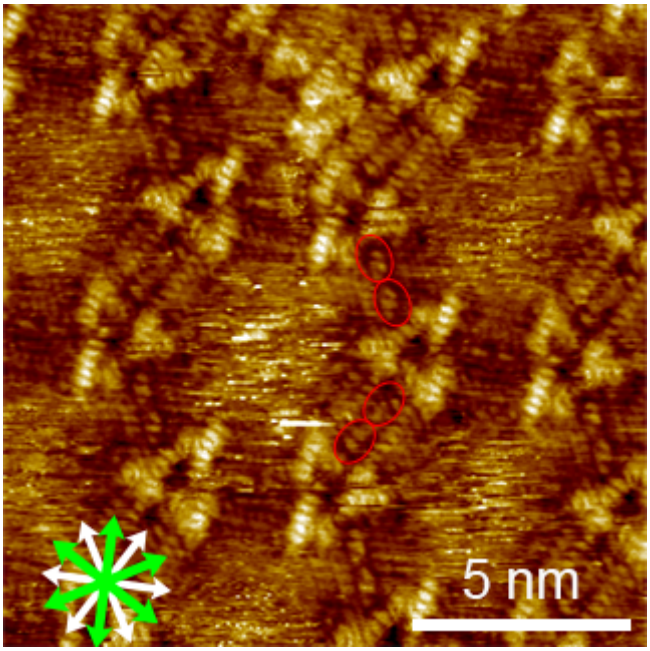

Figure S6. High resolution STM image of a triangular cluster (*n* = 2) structure of **cDBA-OC14(S)-OH** (6.0×10^{-6} M after annealing treatment, I_{set} = 200 pA, V_{bias} = –0.79 V). Red ovals are the HA molecules, respectively.

7-2. STM Images of Chirality of Triangular Cluster Structure at the HA/Graphite Interface

The unit cell parameters of the homochiral CCW triangular cluster (n = 2) structure of **cDBA-OC14(*S*)-OH** at the HA/graphite interface are determined using more than 22 large area STM images (80 nm × 80 nm). Supramolecular chirality is discerned by the angle α value between one of the unit cell vectors and normal $\langle 1\bar{1}00 \rangle$ to one of the main symmetry axes of graphite. 40 data points from five calibrated STM images (30 nm × 30 nm or smaller) are measured. A mean angle α value is –5.0 ± 0.2° (Fig. S7).

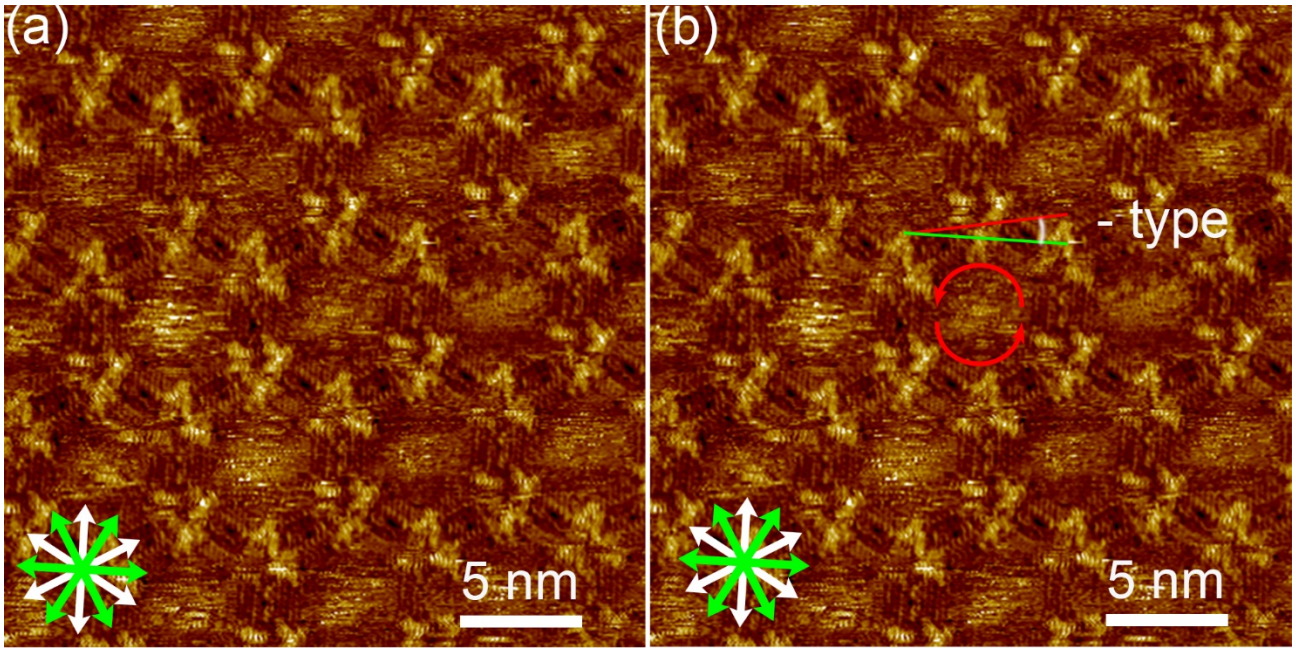

Figure S7. (a, b) STM images of a homochiral triangular cluster (n = 2) structure of **cDBA-OC14(*S*)-OH** at the HA/HOPG interface (1.0×10^{-5} M after annealing treatment, tunneling parameters; I_{set} = 200 pA, V_{bias} = –0.40 V). Red and green lines in (b) are unit cell vector a and one of the normals of the main symmetry axes of graphite respectively.

7-3. Schematic Illustration of Number of Adsorbed Alkoxy Chains per cDBA-OC14(*S*)-OH in Triangular Clusters (*n* = 1, 2, and 4) and Dense Structure

When **cDBA-OC14(*S*)-OH** forms the triangular clusters (n = 1, 2, and 4), the total number of the adsorbed chiral alkoxy chains (m_{total}) per the number of the **cDBA-OC14(*S*)-OH** molecules in the chiral triangular cluster (DBA_{total}) decreases upon increasing its size (m_{total}/DBA_{total} = 3, 2, and 1.2 for n = 1, 2, and 4), as shown in Fig. S8. The m_{total}/DBA_{total} is 0 for the dense structure.

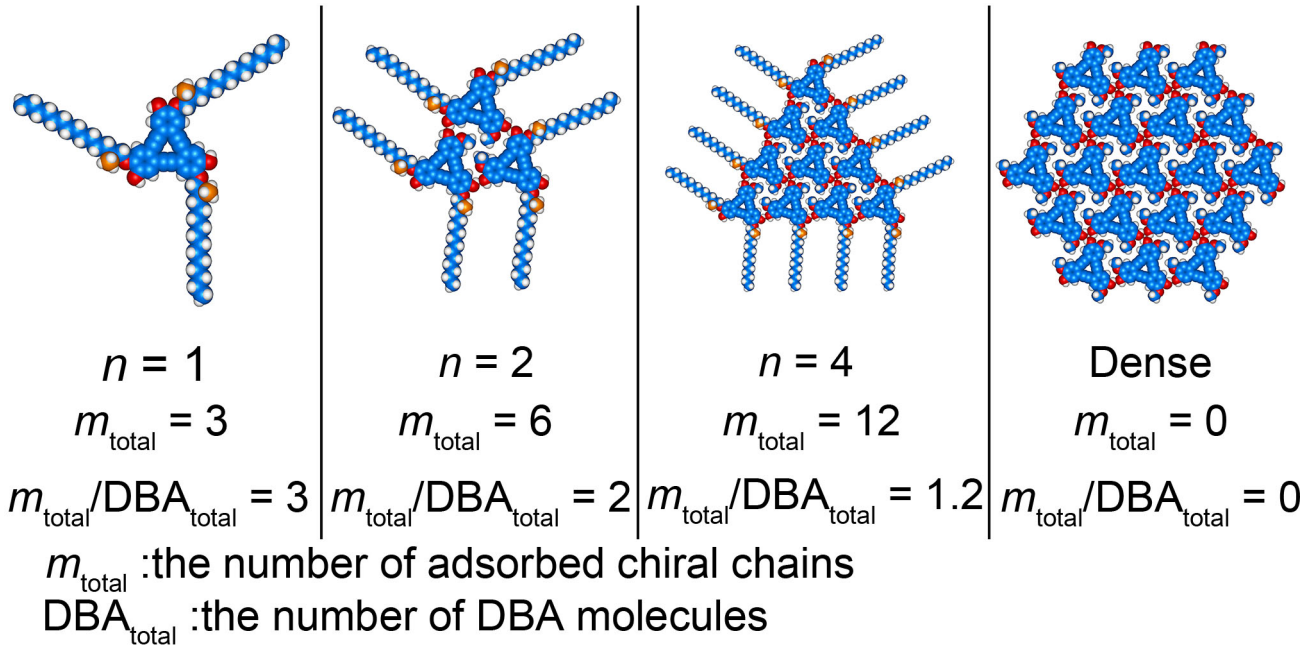

Figure S8. Schematic illustration of the number of adsorbed alkoxy chains per **cDBA-OC14(*S*)-OH** in the triangular clusters (n = 1, 2, 4) and dense structure.

7-4. Additional STM Images of Co-Existing Various Structures at the HA/Graphite Interface

In HA, **cDBA-OC14(*S*)-OH** forms no large domains of the regular structure at the middle concentration range (1.0×10^{-5} to 5.0×10^{-3} M) even after annealing treatment. The triangular clusters with various sizes ($n = 2$ to 4) co-exist without a periodicity together with the domain of a linear structure (Fig. S9).

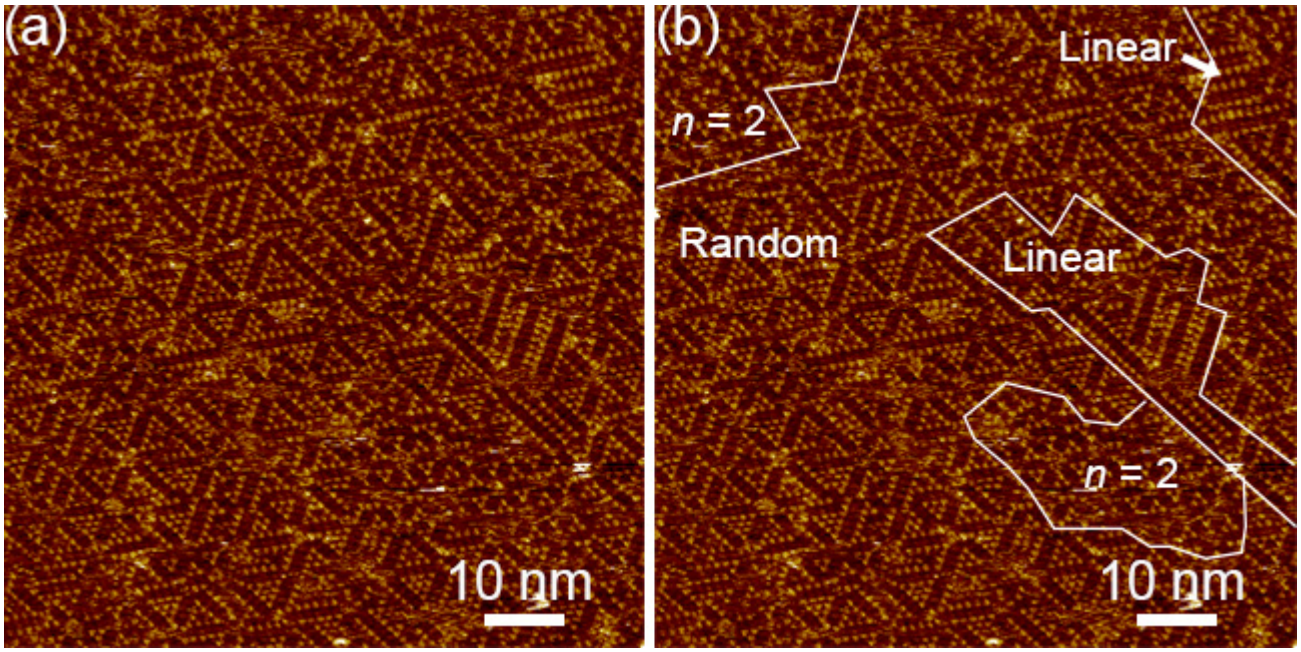

Figure S9. (a, b) STM images of the irregular structure of **cDBA-OC14(*S*)-OH** at a concentration of 1.0×10^{-4} M after annealing treatment (I_{set} = 300 pA, V_{bias} = –0.40 V).

7-5. Additional STM Images of Dense Structure in HA

Just after the annealing treatment, the large domains of the dense structure over 80 nm × 80 nm are observed at the highest concentration (1.0×10^{-2} M) of **cDBA-OC14(*S*)-OH** in HA. The dense structure gradually transforms to a linear structure and disordered area by consecutive STM tip scanning at the same location (Fig. S10).

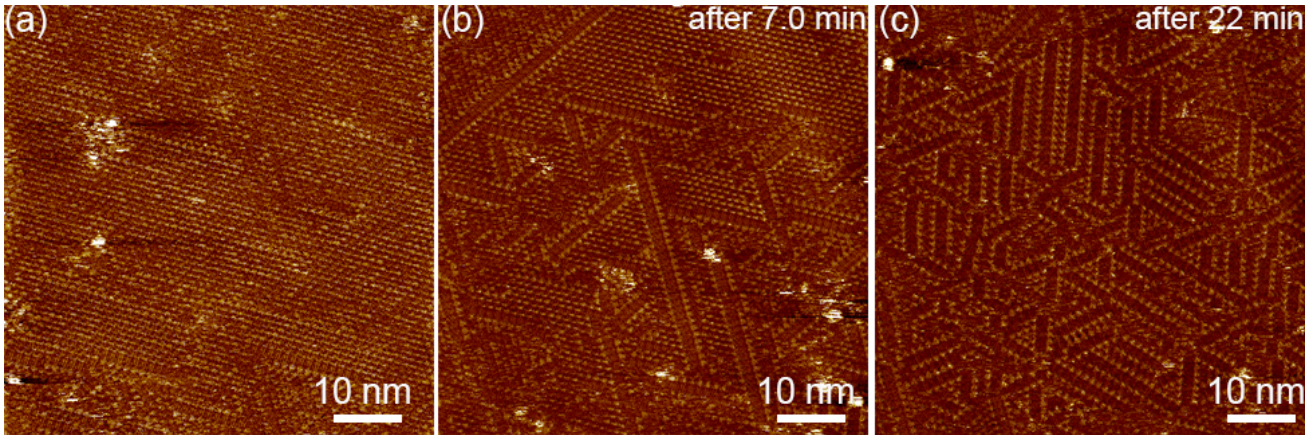

Figure S10. STM images of the SAMNs of **cDBA-OC14(*S*)-OH** recorded during consecutive STM tip scanning at the same location at (a) 0 min, (b) 7 min, and (c) 22 min (1.0×10^{-2} M after annealing treatment, tunneling parameters: I_{set} = 300 pA, V_{bias} = –0.50 V).

7-6. Molecular Models of Chiral Dense Structure

In the STM images of the dense structure, only the triangular π-core of **cDBA-OC14(*S*)-OH** is observed, indicating that all chiral alkoxy chains orient to a solution phase. While there are two chiral configurations of the **cDBA-OC14(*S*)-OH** molecules (*up* and *down* configurations) for the conformational state of $m = 0$ (Fig. S11), only the *up* configuration is observed.

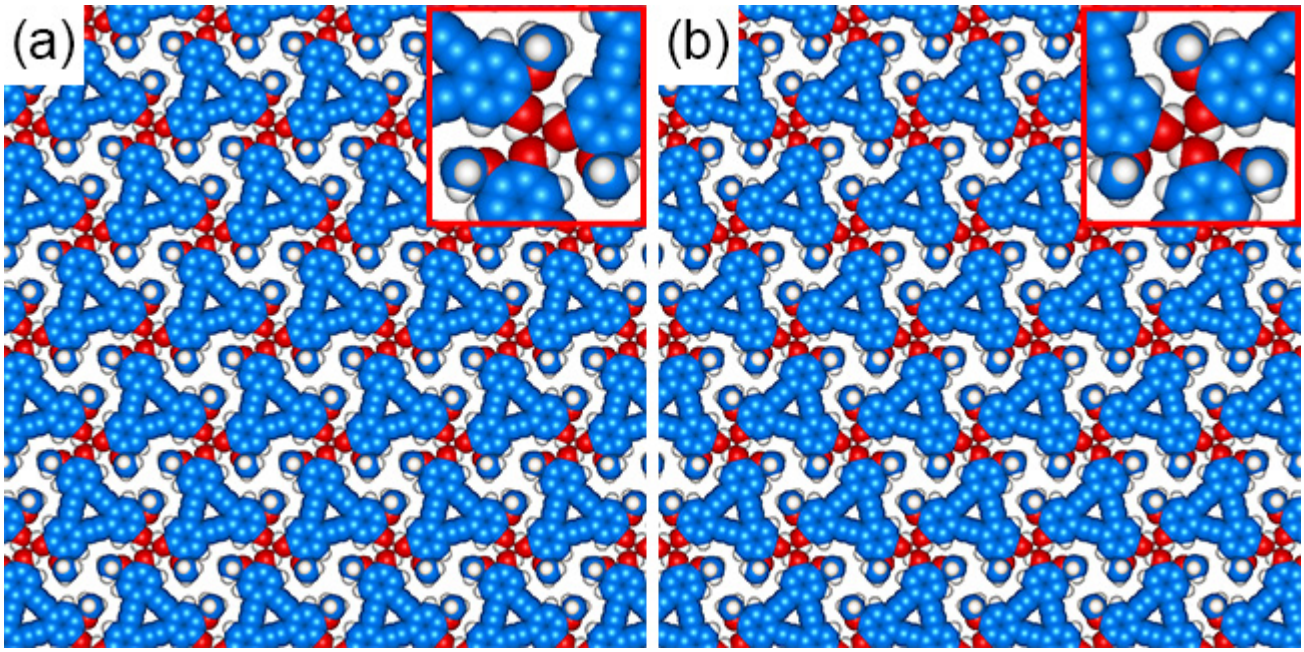

Figure S11. Molecular models of a dense structure optimized by MM calculations on bilayer graphene sheets. The dense structure formed by (a) *down*- and (b) *up*-configurations of **cDBA-OC14(*S*)-OH**. In (a) and (b), the alkoxy chains are omitted for clarity. The bilayer graphene sheets are omitted for clarity.

7-7. Molecular Models of Chiral Dense Structure Formed by cDBA-OC14(*S*)-OH and cDBA-OC14(*R*)-OH

The chiral information of the chains will not be transferred to the dense structure because of their conformational freedom in the solution phase. Indeed, there is no energy difference between the MM-optimized dense structures with the same supramolecular chirality (*S*-configuration) formed by **cDBA-OC14(*S*)-OH** and **cDBA-OC14(*R*)-OH** (Fig. S12).

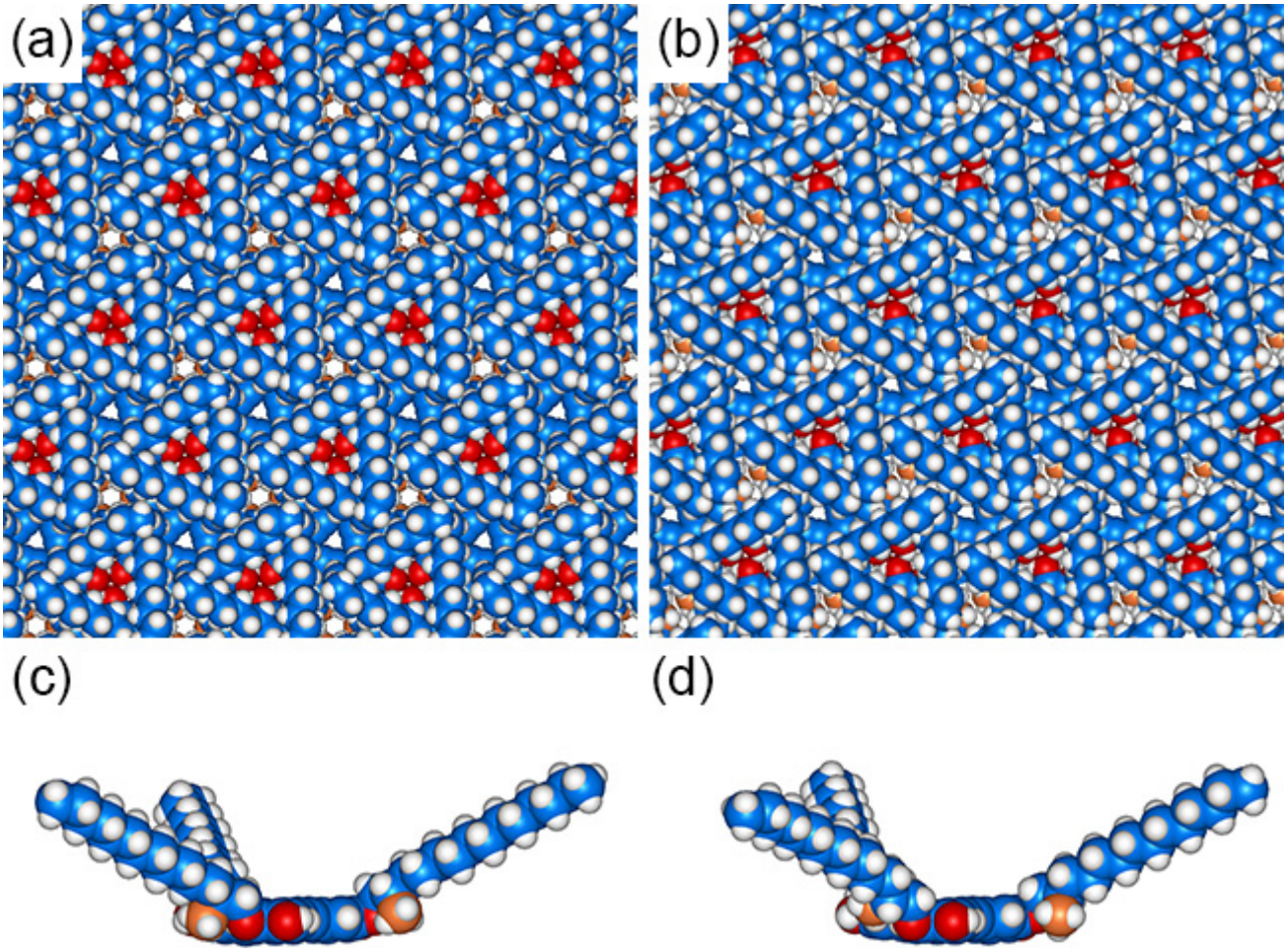

Figure S12. Top and side views of the MM optimized molecular models of the dense structures having the same chirality, yet consisting of different chiral DBA molecules on bilayer graphene sheets. (a, c) **cDBA-OC14(*S*)-OH** with a "*S*-configuration" supramolecular chirality and (b, d) **cDBA-OC14(*R*)-OH** with the same "*S*-configuration" supramolecular chirality.

7-8. Additional STM Images of Linear Structure at a High Concentration Range without Annealing Treatment

Supramolecular chirality of the linear structure is discerned by the angle α value between one of the unit cell vectors and normal $\langle 1\bar{1}00 \rangle$ to one of the main symmetry axes of graphite (Fig. S13). 30 data points from three calibrated STM images (30 nm × 30 nm or smaller) are measured. A mean angle α value is –4 ± 1°.

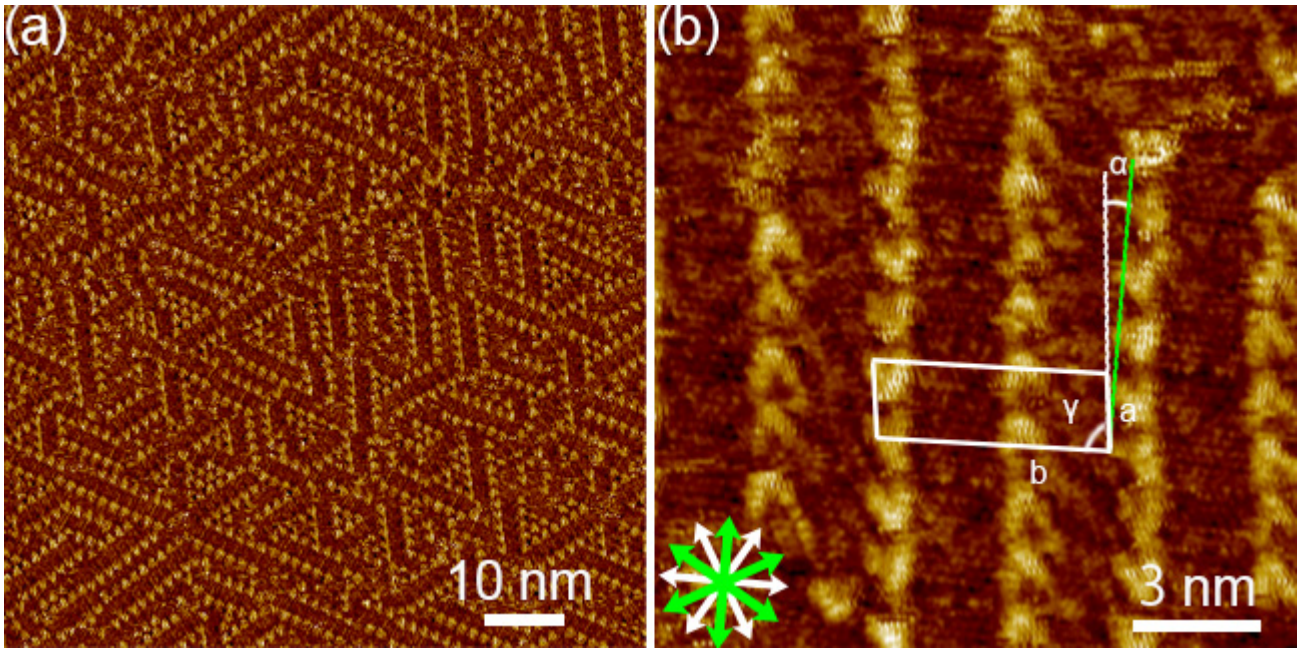

Figure S13. (a, b) STM image of the random and linear structures of **cDBA-OC14(*S*)-OH** at a concentration of 1.0 × 10^{-2} M without annealing treatment (tunneling parameters: I_{set} = 250 pA, V_{bias} = –0.39 V for (a) and I_{set} = 200 pA, V_{bias} = –0.40 V for (b)).

8. **Self-Assembly of cDBA-OC14(*S*)-OH at the Interface between a Mixture of HA and TCB and Graphite**

8-1. Additional STM Images of Triangular Cluster (*n* = 4)

A triangular cluster (*n* = 4) is composed of nine **cDBA-OC14(S)-OH** molecules (Fig. S14a). However, in many clusters, the central **cDBA-OC14(S)-OH** molecule (blue dotted triangles in Fig. S14b) adopting the conformational state *m* = 0 is often missing. Eight alkoxy chains of **cDBA-OC14-OH** and six short alkyl units of HA (red ovals in Fig. S14b) are observed between the adjacent triangular clusters.

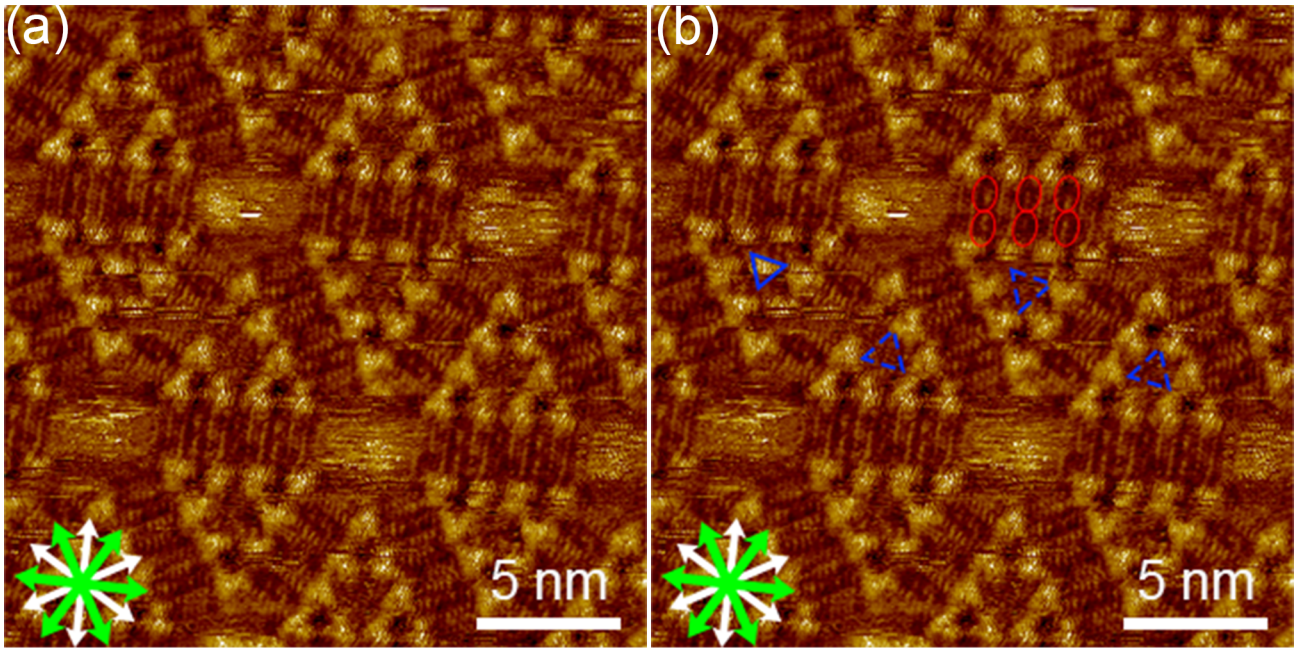

Figure S14. (a, b) STM images of a triangular cluster (*n* = 4) structure of **cDBA-OC14(*S*)-OH** (X_{HA} = 0.80, tunneling parameters: I_{set} = 260 pA, V_{bias} = –0.51 V).

8-2. STM Images of SAMNs of cDBA-OC14(*S*)-OH Taken at $C = 5.39 \times 10^{-4}$ M and $X_{HA} = 0.90$

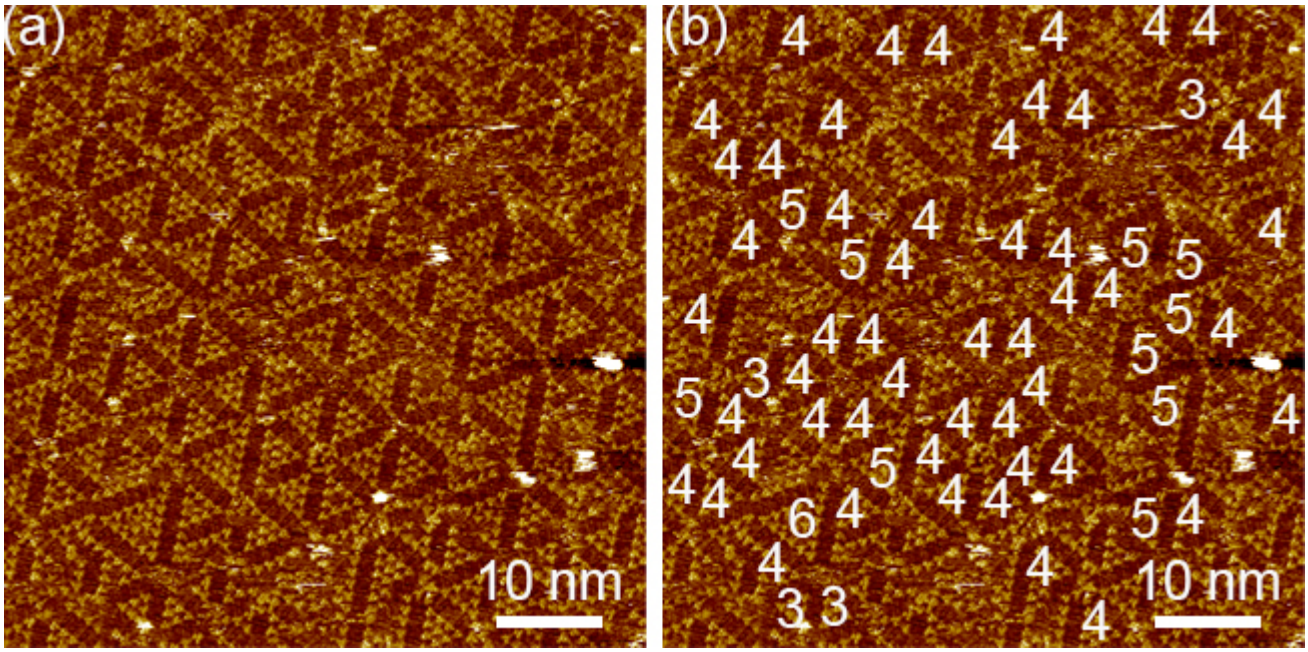

Figure S15. (a, b) STM images of hierarchical triangular cluster (n = 3 to 6) structures (X_{HA} = 0.90 after annealing treatment, I_{set} = 200 pA, V_{bias} = –0.40 V). In (b), numbers corresponding to n are overlayed.

8-3. STM Images of SAMNs of cDBA-OC14(*S*)-OH Observed at $C = 1.02 \times 10^{-2}$ M and $X_{HA} = 0.99$

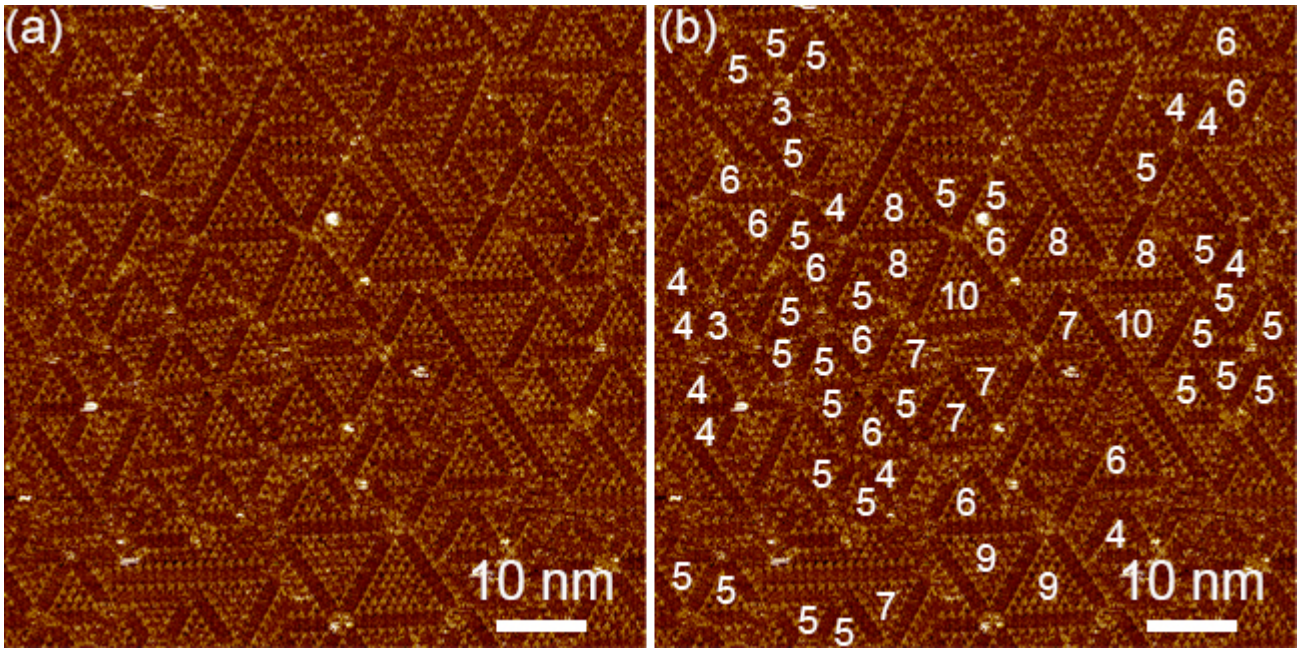

Figure S16. (a, b) STM images of hierarchical triangular cluster (n = 3 to 10) structures (X_{HA} = 0.99 after annealing treatment, I_{set} = 230 pA, V_{bias} = –0.40 V). In (b), numbers corresponding to n are overlayed.

8-4. Chirality Analysis at Triangular Cluster Level

Supramolecular chirality at a triangular cluster level is analyzed for the hierarchical triangular cluster structures composed of various triangular clusters with different sizes. For this purpose, we measure the angle β value between one of the sides of the triangle cluster and one of the normals of the main symmetry axes of graphite underneath (Fig. S17). The angle β values are all negative with a mean value of –5°.

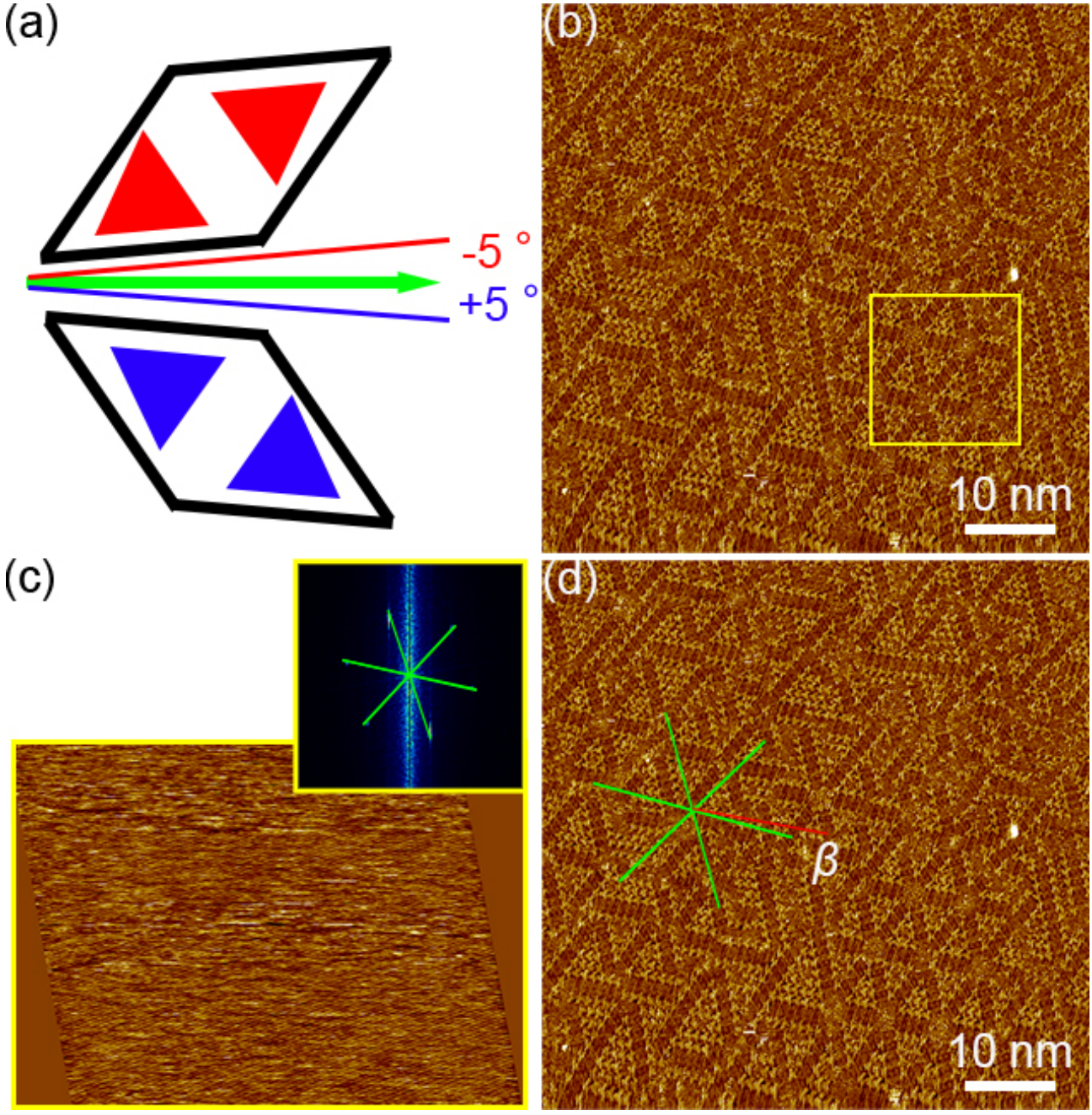

Figure S17. (a) Schematic drawing showing supramolecular chirality at each triangular cluster level. The side of the

triangular cluster is tilted ±5°. When the chiral configuration is controlled, only positive or negative values should be determined. (b, d) Triangular cluster (n = 2 to 10) structures (4.5×10^{-3} M, X_{HA} = 0.90 after annealing treatment, I_{set} = 250 pA, V_{bias} = –0.60 V). (c) STM image of a graphite surface underneath at a yellow square area in (b) for determination of the normals to the main symmetry axes of graphite (X_{HA} = 0.90 after annealing treatment, I_{set} = 250 pA, V_{bias} = –0.02 V). In (c), the inset corresponds to the 2D-FFT image. Green lines are the normals of the main symmetry axes of graphite. In (d), the red line is parallel to one of the sides of the triangle cluster.

8-5. Combinations of Molecular Conformations which Construct Hierarchical SAMNs

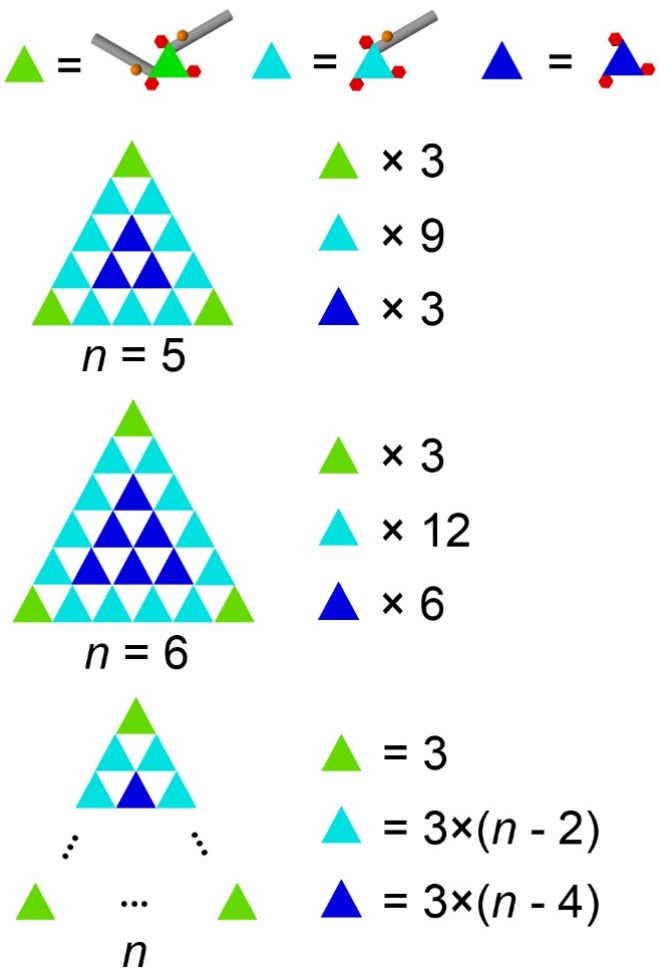

Figure S18. The number and combinations of molecular conformations for several sizes of triangular clusters.

9. **Self-Assembly of cDBA-OC14(*R*)-OH at the TCB/Graphite Interface**

At the TCB/graphite interfaces, a homochiral honeycomb structure (CW orientation) of **cDBA-OC14(*R*)-OH** is solely observed at all solute concentrations (Fig. S19).

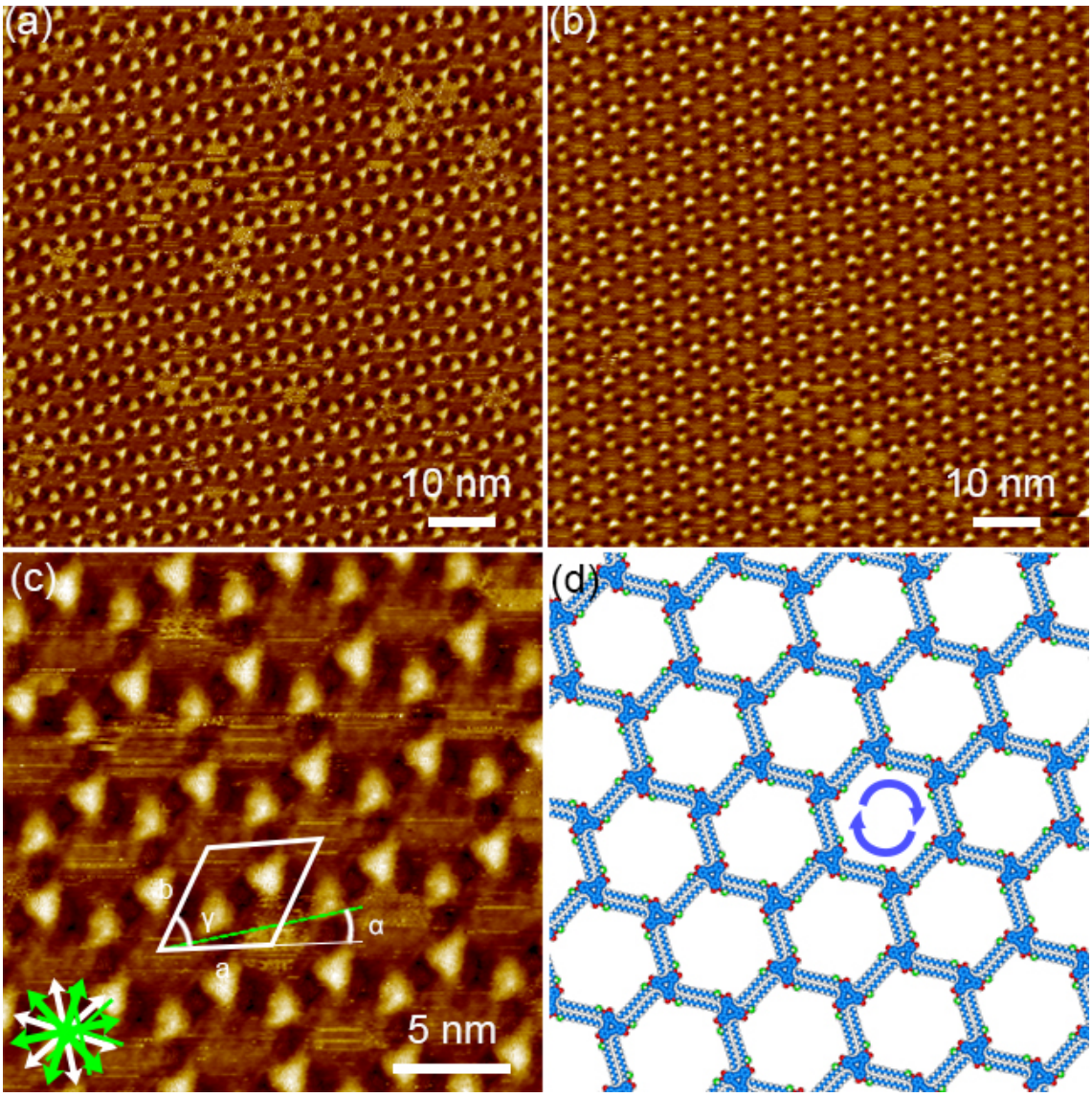

Figure S19. STM images of a homochiral honeycomb structure (a) at 3.0×10^{-6} M after annealing treatment (I_{set} = 230 pA, V_{bias} = –0.51 V) and (b) at 1.0×10^{-4} M after annealing treatment (I_{set} = 210 pA, V_{bias} = –0.44 V). (c) STM image of a honeycomb structure (3.0×10^{-6} M, I_{set} = 220 pA, and V_{bias} = −0.52 V) and (d) corresponding molecular models optimized by MM calculation on bilayer graphene sheets. In the MM models in (d), the bilayer graphene sheets were omitted for clarity. Color codes in (b): blue; carbon atoms of **cDBA-OC14(*R*)-OH**, green; carbon atoms of the methyl groups attached to the stereogenic centers, red; oxygen atoms, and white; hydrogen atoms.

10. **Self-Assembly of cDBA-OC14(*R*)-OH at the HA/Graphite Interface**

At a low solute concentration of 6.0×10^{-6} M, a homochiral triangular cluster structure ($n = 2$, CW orientation) of **cDBA-OC14(*R*)-OH** is observed. At the highest concentration of 1.0×10^{-2} M, a homochiral densely packed structure of **cDBA-OC14(*R*)-OH** is observed.

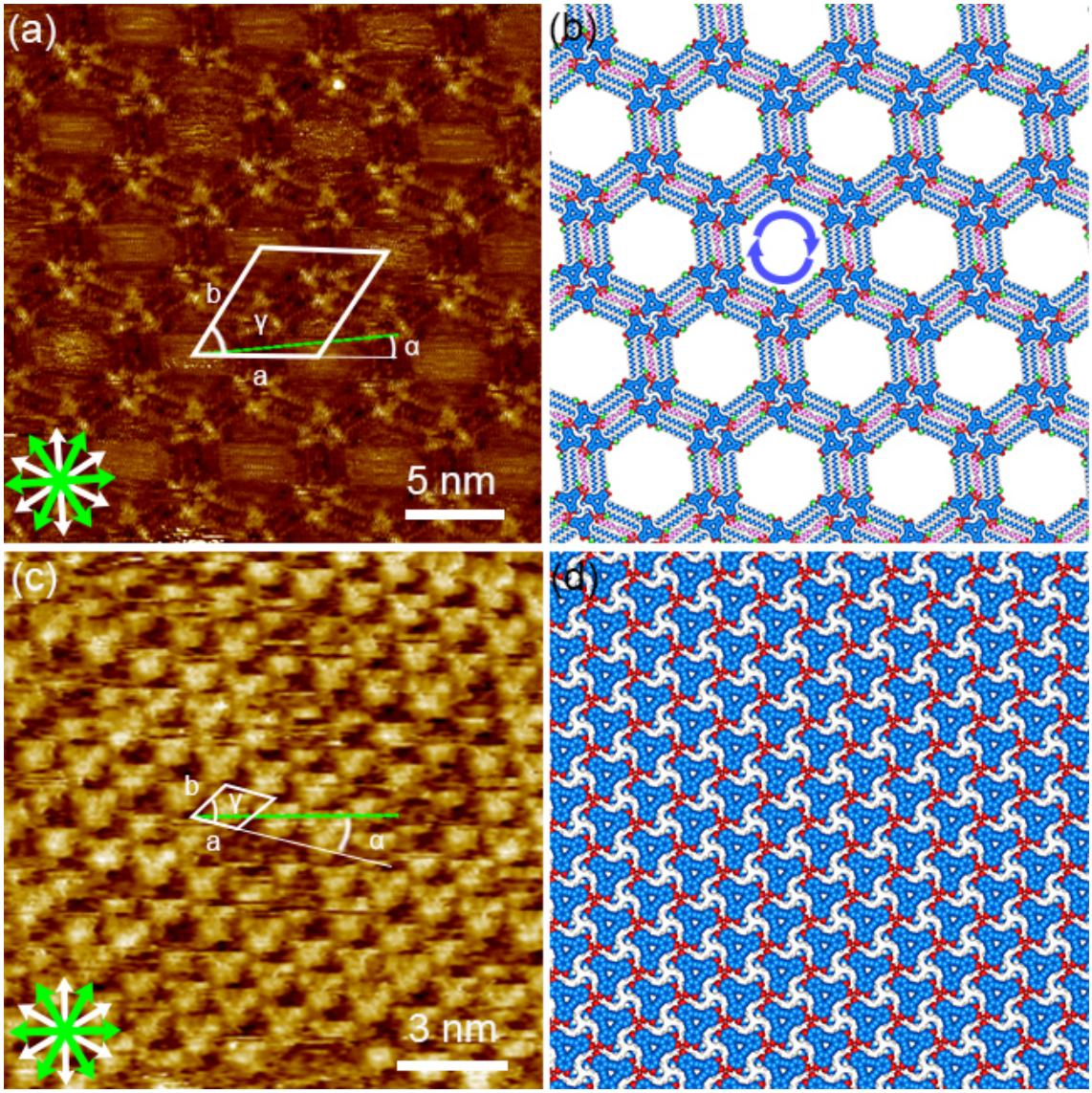

Figure S20. SAMNs formed by **cDBA-OC14(*R*)-OH** at the HA/graphite interface after annealing treatment. (a) STM image of a triangular cluster ($n = 2$, 6.0×10^{-6} M, $I_{set} = 220$ pA, and $V_{bias} = -0.52$ V) and (c) STM image of a dense structure (1.0×10^{-2} M, $I_{set} = 230$ pA, and $V_{bias} = -0.82$ V). (b, d) corresponding molecular models optimized by MM calculation on bilayer graphene sheets. In the MM models, the bilayer graphene sheets and the alkoxy chains of the cDBA molecules orienting to the solution phase were omitted for clarity.

11. **Self-Assembly of cDBA-OC14(*R*)-OH at the Interfaces between a Mixture of HA and TCB and Graphite**

11-1. Additional STM Images of Homochiral Triangular Cluster (*n* = 4, CW Orientation)

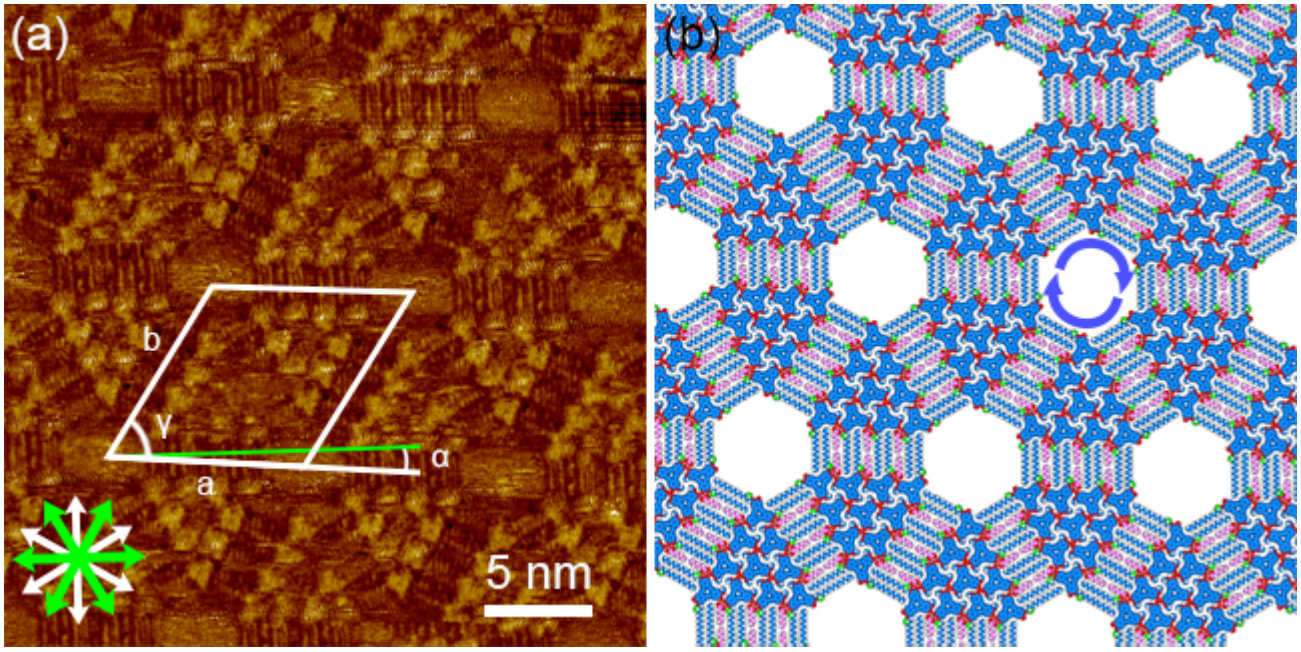

Figure S21. STM images of a homochiral triangular cluster structure (*n* = 4, CW orientation) (a) at 5.0×10^{-4} M and X_{HA} = 0.80 after annealing treatment (I_{set} = 230 pA, V_{bias} = –0.62 V) and (b) corresponding molecular models optimized by MM calculation on bilayer graphene sheets. In the MM models in (b), the bilayer graphene sheets were omitted for clarity. Color codes in (b): blue; carbon atoms of **cDBA-OC14(*R*)-OH**, green; carbon atoms of the methyl groups attached to the stereogenic centers, red; oxygen atoms, and white; hydrogen atoms.

11-2. STM Image of Triangular Cluster Structures of cDBA-OC14(*R*)-OH Taken at $C = 5.4 \times 10^{-4}$ M and $X_{HA} = 0.80$

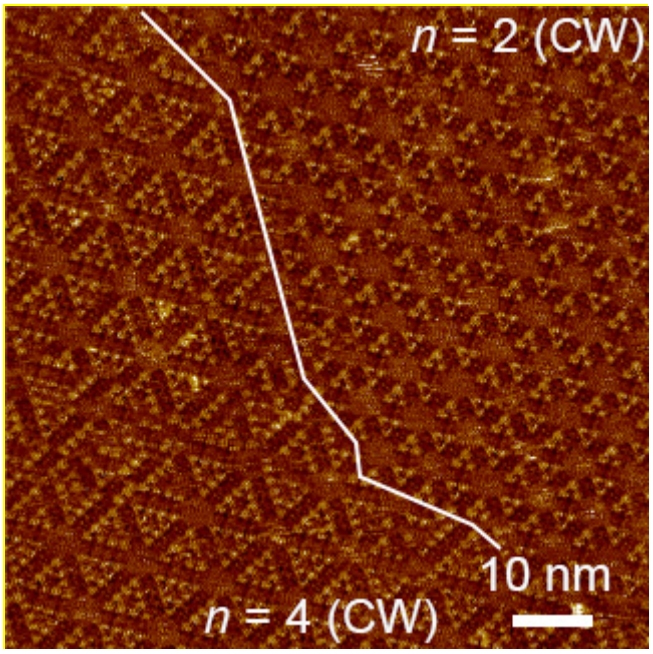

Figure S22. STM images of homochiral hierarchical triangular cluster (n = 2 and 4) structures formed by **cDBA-OC14(*R*)-OH** at an X_{HA} of 0.80 at a concentration of 5.4×10^{-4} M after annealing treatment (I_{set} = 240 pA, V_{bias} = –0.50 V).

11-3. STM Images of Triangular Cluster Structures of cDBA-OC14(*R*)-OH Taken at $C = 1.0 \times 10^{-2}$ M and X_{HA} = 0.99

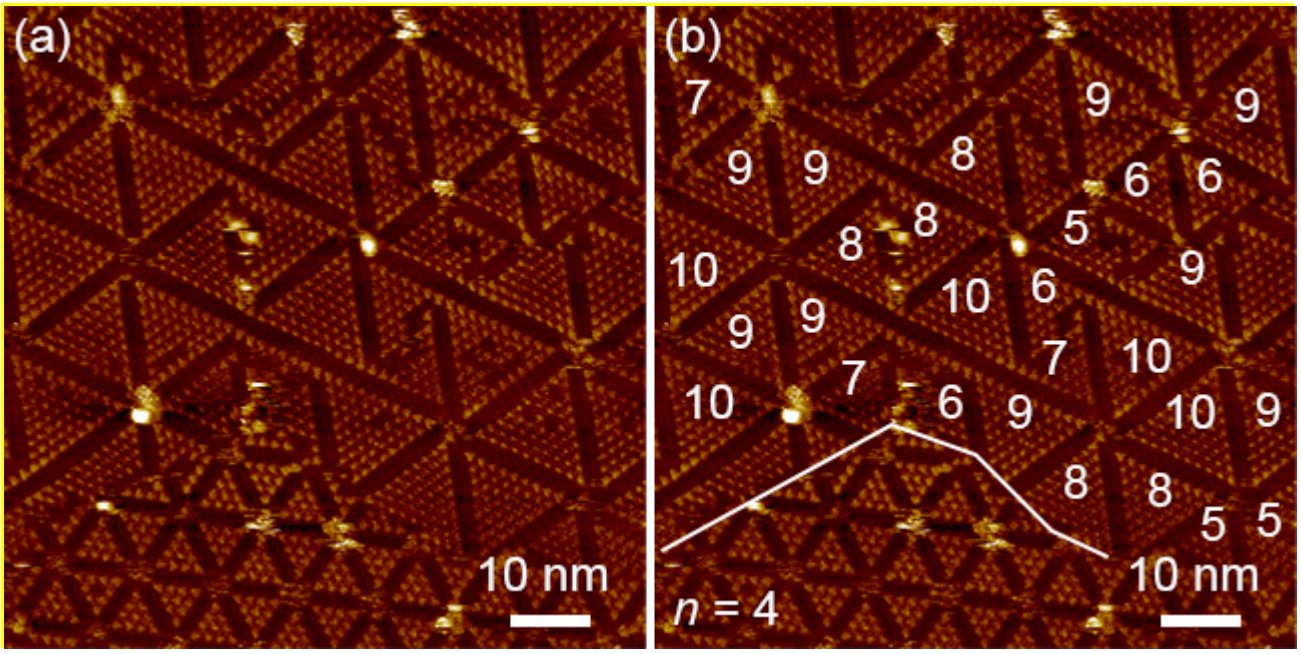

Figure S23. (a, b) STM images of hierarchical triangular cluster (n = 4 to 10) structures formed by **cDBA-OC14(*R*)-OH** (X_{HA} = 0.99 after annealing treatment, I_{set} = 250 pA, V_{bias} = –0.42 V). In (b), numbers corresponding to n are overlayed.

12. **Unit Cell Parameters of the Self-Assembled Patterns of cDBA-OC14(*R*)-OH**

The unit cell parameters and angle α values of self-assemblies of **cDBA-OC14(*R*)-OH** at different conditions are summarized in Table S2. The unit cell parameters and angle α values are determined using more than 50 points from more than five STM images. The mean angle α values are all positive. These results imply that the SAMNs of **cDBA-OC14(*R*)-OH** are homochiral.

Table S2. Summary of Unit Cell Parameters and Angle α Values of Observed SAMNs of **cDBA-OC14(*R*)-OH**.

SAMN	unit cell parameters and angle α value			
	a (nm)	*b* (nm)	γ (°)	α (°)
honeycomb	5.10 ± 0.06	5.03 ± 0.09	59.8 ± 0.7	9.7 ± 0.8
triangular cluster (*n* = 2)	6.40 ± 0.09	6.39 ± 0.09	60.0 ± 0.6	4.8 ± 0.5
dense	1.37 ± 0.09	1.39 ± 0.07	60.1 ± 0.5	18.0 ± 1.2
triangular cluster (*n* = 4)	9.22 ± 0.15	9.21 ± 0.11	60.1 ± 0.6	4.7 ± 0.5

13. **Solvation Energies Estimated by MD Simulations**

Molecular dynamics (MD) simulations were performed by the canonical (NVT) ensemble at 298 K using the Nose-Hoover thermostat with the integration time step of 1 fs. The solvation energies of **cDBA-OC14(*S*)-OH** in HA is calculated by MD simulation using the solvation free energy tools in the Forcite module. Three-dimensional solvent boxes with periodic boundary conditions (a = 40 Å, b = 40 Å, c = 50 Å and α = β = γ = 90°) including 400 HA molecules are used. Before the solvation energy calculation, solvent phases were equilibrated by MD simulations. Then, one chiral DBA molecule is added to the solvent boxes and the four or six solvent molecules are removed from the solvent boxes. The systems are equilibrated again by MD simulations. When the potential energy change becomes less than 5 kcal/mol in 1 ns, we judged that the system reaches the equilibrium. The solvation energies are calculated using the following equation: $E_{solv} = E_{vacuum} + E_{van\ der\ Waals} + E_{electrostatic}$. The solvation energy of **cDBA-OC14(*S*)-OH** in HA is –2.45 kcal/mol, which is smaller than that of **DBA-OC14-OH** (–0.26 kcal·mol^{-1}, Table S3).[4]

Table S3. Summary of MD Simulations.

solute molecule	solvent	number of solvent molecules	density (g/cm^3)	E_{vacuum}[a] (kcal/mol)	$E_{van\ der\ Waals}$[b] (kcal/mol)	$E_{electrostatic}$[c] (kcal/mol)	E_{solv}[d] (kcal/mol)
DBA-OC14-OH[e]	HA	396	0.933	–3.65	–5.15	–1.77	–0.26
		394	0.924	–3.38	–5.11	-0.29	–1.44
DBA-OC14(*S*)-OH	HA	396	0.933	–4.79	–4.79	–1.18	–2.45
		394	0.924	–5.75	–13.78	6.23	–13.29

[a] Energy of the DBA molecule in vacuum. The molecular configuration is identical to that in the solvated structure. [b] Van der Waals contribution in the solvate structure. [c] Electrostatic contribution in the solvate structure. [d] The total solvation free energy. This was calculated by the following equation $E_{solv} = E_{vacuum} + E_{van\ der\ Waals} + E_{electrostatic}$. [e] The values of **DBA-OC14-OH** were reported in Ref. 4.

14. ^{1}H and ^{13}C NMR Spectra of New Compounds

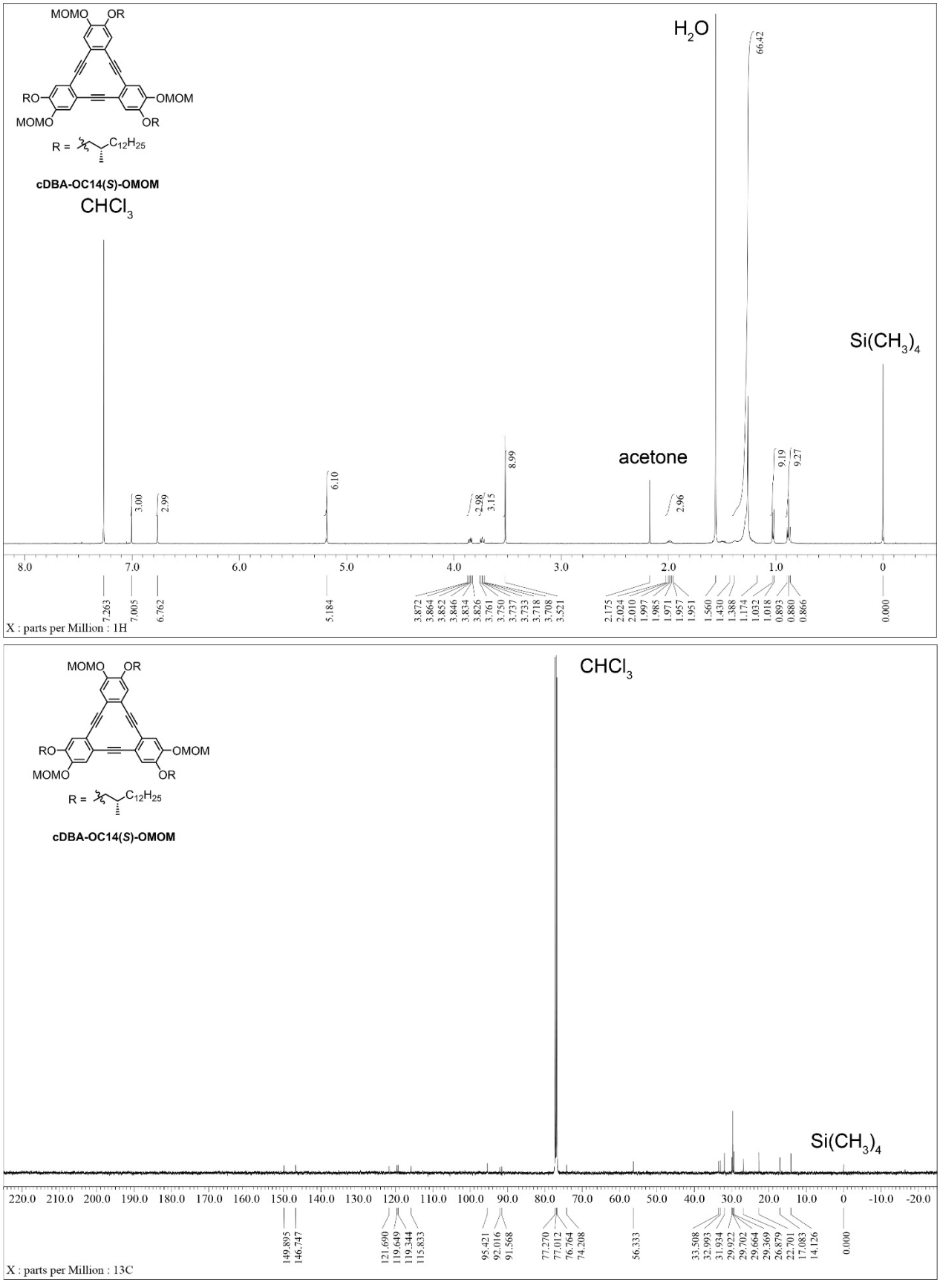

Figure S24. ^{1}H and ^{13}C NMR spectra of **cDBA-OC14(*S*)-OMOM** in $CDCl_3$ at 25 °C.

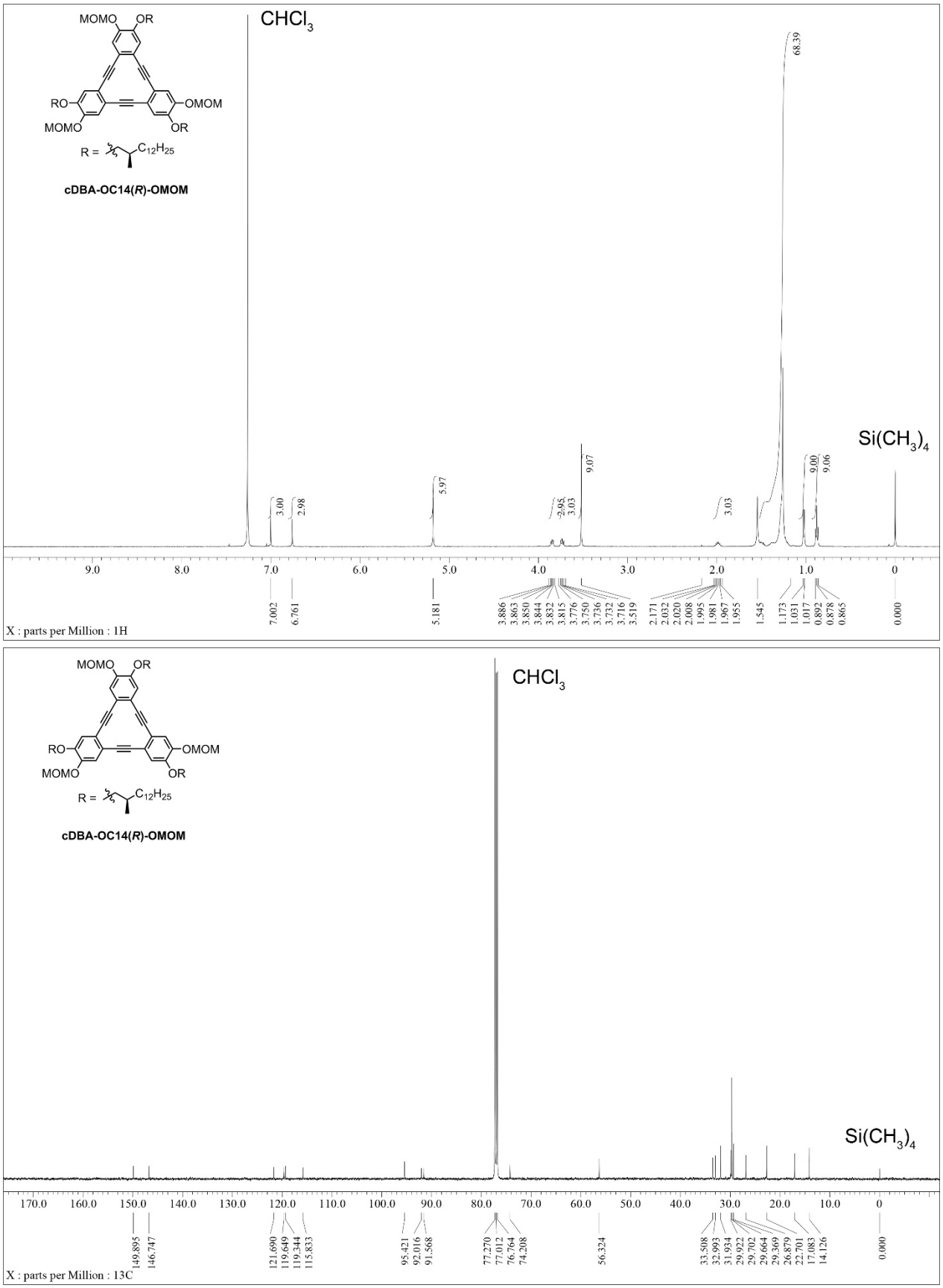

Figure S25. ^{1}H and ^{13}C NMR spectra of **cDBA-OC14(*R*)-OMOM** in $CDCl_3$ at 25 °C.

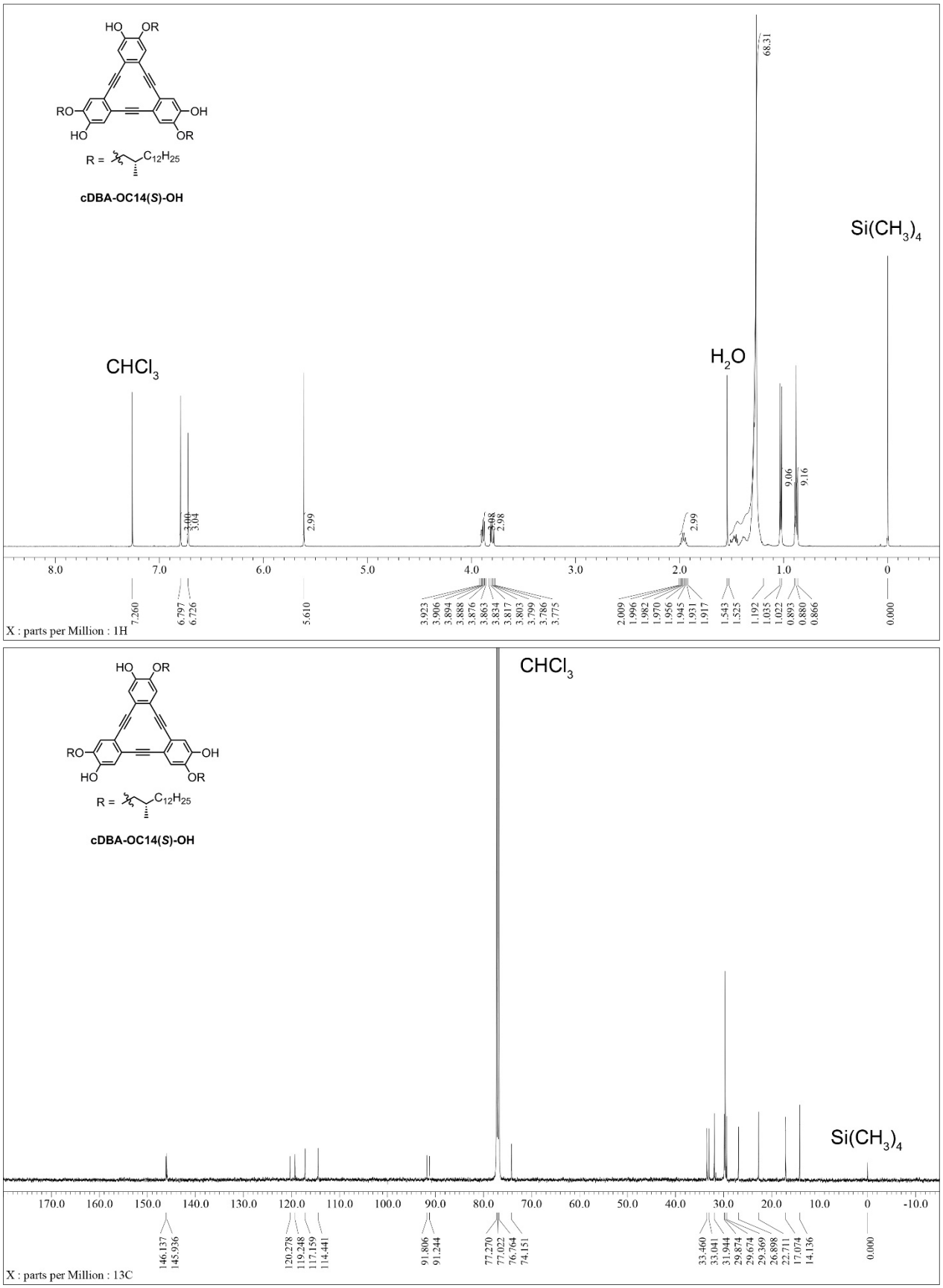

Figure S26. ^{1}H and ^{13}C NMR spectra of **cDBA-OC14(*S*)-OH** in $CDCl_3$ at 25 °C.

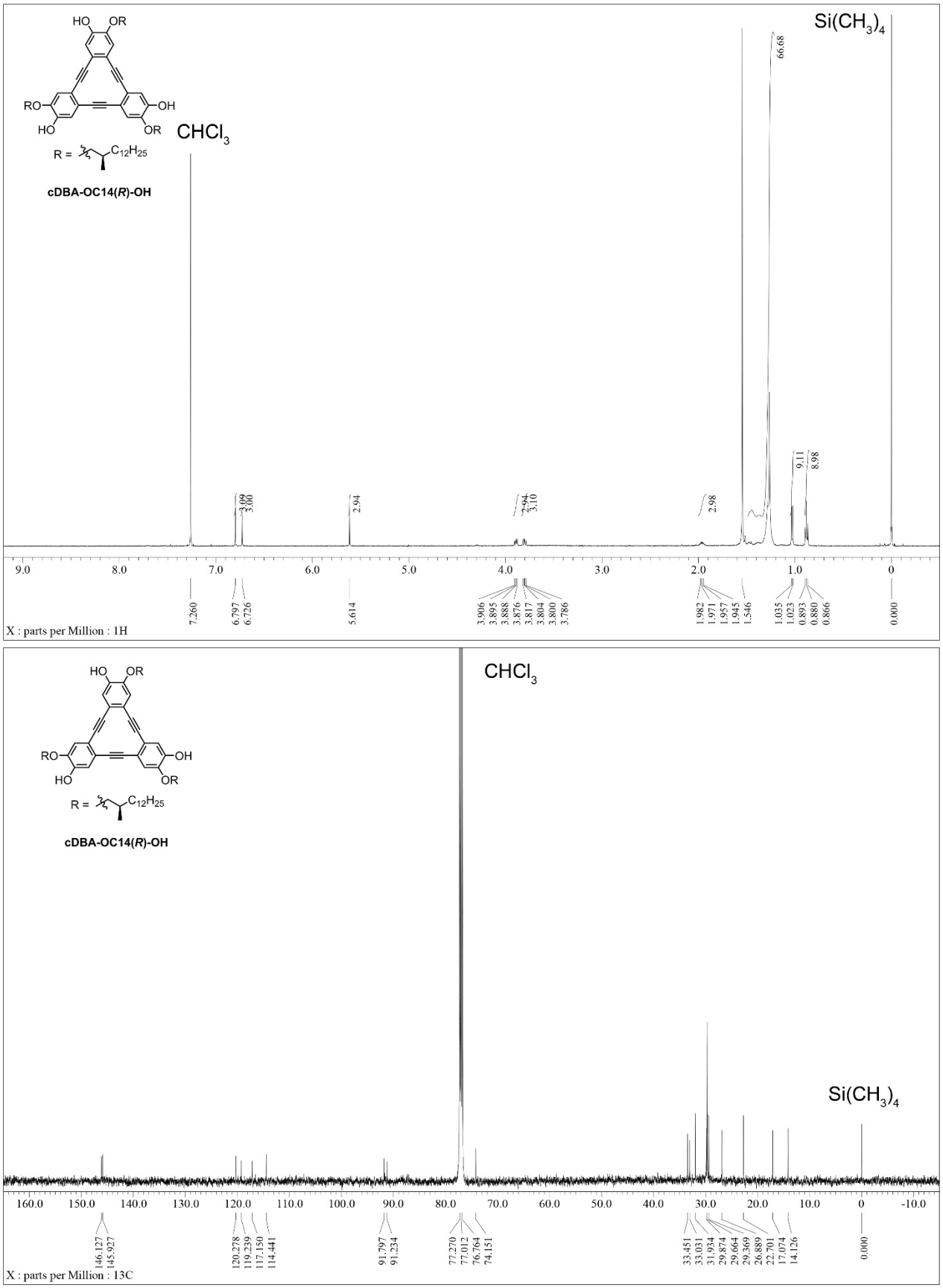

Figure S27. ^{1}H and ^{13}C NMR spectra of **cDBA-OC14(*R*)-OH** in $CDCl_3$ at 25 °C.

15. **References**

1. Tahara, K.; Yamaga, H.; Ghijsens, E.; Inukai, K.; Adisoejoso, J.; Blunt, M. O.; De Feyter, S.; Tobe, Y. Control and Induction of Surface-Confined Homochiral Porous Molecular Networks. *Nat. Chem.* 2011, **3**, 714−719.

2. Tahara, K.; Kubo, Y.; Hashimoto, S.; Ishikawa, T.; Kaneko, H.; Brown, A.; Hirsch, B. E.; De Feyter, S.; Tobe, Y. Porous Self-Assembled Molecular Networks as Templates for Chiral Position-Controlled Chemical Functionalization of Graphitic Surfaces. *J. Am. Chem. Soc.* 2020, **142**, 7699–7708.

3. Yuan, G.; Yang, Y.; Liu, J.; Bian, Q.; Wang, M.; Zhong, J. Synthesis of the Enantiomers of 13-Methylheptacosane, the Sex Pheromone of Pear Psylla, Cacopsylla Pyricola. *Chirality*, 2021, **33**, 274–280.

4. Maeda, M.; Nakayama, R.; De Feyter, S.; Tobe, Y.; Tahara, K. Hierarchical Two-Dimensional Molecular Assembly through Dynamic Combination of Conformational States at the Liquid/Solid Interface. *Chem. Sci*. 2020, **11**, 9254–9261.